Biogeosciences, 22, 181–212, 2025
https://doi.org/10.5194/bg-22-181-2025

Biogeosciences Open Access EGU

Development of the DO_3SE-Crop model to assess ozone effects on crop phenology, biomass, and yield

Pritha Pande[1], Sam Bland[1], Nathan Booth[2], Jo Cook[2], Zhaozhong Feng[3], and Lisa Emberson[2]

[1]Stockholm Environment Institute at York, Department of Environment and Geography, University of York, YO10 5DD, York, UK
[2]Department of Environment and Geography, University of York, YO10 5DD, York, UK
[3]Key Laboratory of Agrometeorology of Jiangsu Province, School of Ecology and Applied Meteorology, Nanjing University of Information Science and Technology, Nanjing, China

Correspondence: Pritha Pande (pritha.pande@york.ac.uk)

Received: 7 March 2024 – Discussion started: 16 April 2024
Revised: 23 October 2024 – Accepted: 25 October 2024 – Published: 10 January 2025

Abstract. A substantial body of empirical evidence exists to suggest that elevated O_3 levels are causing significant impacts on wheat yields at sites representative of highly productive arable regions around the world. Here we extend the DO_3SE model (designed to estimate total and stomatal O_3 deposition for risk assessment) to incorporate a coupled A_{net}–g_{sto} model to estimate O_3 uptake; an O_3 damage module (that impacts instantaneous A_{net} and the timing and rate of senescence); and a crop phenology, carbon allocation, and growth model based on the JULES-crop model. The model structure allows scaling from the leaf to the canopy to allow for multiple leaf populations and canopy layers. The DO_3SE-Crop model is calibrated and parameterised using O_3 fumigation data from Xiaoji, China, for the year 2008 and for an O_3-tolerant and sensitive cultivar. The calibrated model was tested on data for different years (2007 and 2009) and for two additional cultivars and was found to simulate key physiological variables, crop development, and yield with a good level of accuracy. The DO_3SE-Crop model simulated the phenological stages of crop development under ambient and elevated O_3 treatments for the test datasets with an R^2 of 0.95 and an RMSE of 2.5 d. The DO_3SE-Crop model was also able to simulate O_3-induced yield losses of $\sim$ 11 %–19 % compared to observed yield losses of 12 %–34 %, with an R^2 of 0.68 ($n = 20$) and an RMSE of 76 g m^{-2}. Additionally, our results indicate that the variance in yield reduction is primarily attributed to the premature decrease in carbon assimilation to the grains caused by accelerated leaf senescence, which is brought forward by 3–5 d under elevated O_3 treatments.

1 Introduction

Ground-level ozone (O_3) is considered the most critical air pollutant causing global damage to agricultural crops. Elevated O_3 concentrations are particularly problematic in Asia, where decades of rapid economic growth, industrialisation, and urbanisation have seen sharp rises in pollutant emissions associated with burning fossil fuels (Lin et al., 2017), causing substantial O_3-induced crop yield losses across the region (Z. Feng et al., 2022). At the same time, climate change is considered a substantial threat to arable productivity through changes in average and extreme temperature and precipitation profiles across the region (IPCC, 2021). Reductions in precipitation are considered responsible for poor harvests in recent years (Liu et al., 2010), and rising temperatures that reduce the length of the crop growing season are thought to have caused losses in crop yield (Malhi et al., 2021). There is now substantial evidence showing that stresses from O_3 pollution and climate variability interact, causing either additive, synergistic, or antagonistic responses in crop development, growth, and yield (Sillmann et al., 2021). The threat posed by these stresses is a particular cause for concern in Asia since the continent contributes approximately 43 % of the global wheat production, with China contributing the highest production levels at 17 % of the global wheat supply (Feng et al.,

2021). O_3 levels are rising substantially in important wheat-growing areas in China such as the North China Plain and the Yangtze River Delta (Li et al., 2020; Zhang et al., 2023). Concern over O_3 impacts led to the implementation in 2013 of a range of policies to try to reduce O_3 precursor emissions across China. These included a comprehensive management plan to control volatile organic compounds (VOCs) from key industries, an atmospheric pollution prevention and control law of the People's Republic of China, and a 2020 VOC management plan (Li et al., 2021). As a result, nitrogen oxide (NO_x) emissions, an important O_3 precursor, have decreased by 21 % from 2013 to 2017 (Li et al., 2021). By contrast, VOCs have only slightly decreased by 2 % over the same period. Since China has a VOC-limited O_3 regime, the reductions in NO_x lead to rather insignificant changes in O_3 concentration (Li et al., 2021), though evidence suggests that reductions in O_3 may be higher in rural areas than in urban areas (Lee et al., 2020). This implies future policies to tackle ground-level O_3 pollution in China need to increase their focus on reducing VOCs along with NO_x (Lee et al., 2020) and also emphasise the importance of being able to make assessments of O_3 damage to key receptors such as staple crops.

At present, methods to assess the risk to crop productivity from changes in O_3 and climate variables use a variety of different O_3 risk assessment methods (Ronan et al., 2020) and crop models as discussed in depth in Emberson et al. (2018). In the past, O_3 risk assessment methods relied heavily on dose–response relationships, empirically derived relationships that assess changes in a response variable (most commonly yield) against an O_3 exposure metric (concentration or, more recently, flux-based indices) (Pleijel et al., 2022). By contrast, methods to assess the impact of climate variables (most commonly changes in temperature, precipitation, and CO_2 concentration) tend to use crop models since these allow the integration of the combined effect of a number of different variables acting simultaneously to affect crop development, growth, and yield (Schauberger et al., 2019). A new generation of crop models that include O_3 damage are now being developed and applied and have the potential to estimate the combined effect of O_3 and climate variables on crop development, biomass, and yield. Such models can arguably be classified into two types of crop model: firstly, those that rely on O_3 metrics (e.g. AOT40 or M7) to modify crop growth determined by radiation use efficiency (Guarin et al., 2019, 2024) or evapotranspiration (Droutsas et al., 2020); secondly, those that estimate stomatal O_3 uptake to modify crop growth determined by photosynthesis and subsequent carbon assimilation (Tao et al., 2017; Schauberger et al., 2019; Nguyen et al., 2024). The DO_3SE-Crop model falls into the latter category of photosynthesis-based crop models and was developed to bridge the gap between O_3 risk assessment modelling methods and crop models.

The DO_3SE model is an O_3 deposition model that can be embedded within atmospheric chemistry transport models (e.g Simpson et al., 2012) and uses either a multiplicative or coupled A_{net}–g_{sto} model to estimate stomatal O_3 flux (Pande et al., 2024). The accumulated stomatal O_3 flux has been successfully used as a damage metric (POD_y – phytotoxic ozone dose over a threshold y; LRTAP, 2017) to predict O_3-induced yield loss (Pande et al., 2024). The ability of the DO_3SE model to simulate A_{net}, as well as the inclusion of a process-based O_3 damage module for both instantaneous A_{net} and early and enhanced senescence (after Ewert and Porter, 2000), lends itself to the development of the DO_3SE model as a process-based crop model. The inclusion of resistance algorithms that can assess the transport of O_3 concentrations from a reference height above a canopy down to the canopy top means the model can be embedded within existing atmospheric chemistry transport schemes and hence applied to regional- or global-scale O_3 risk assessment whilst also modelling O_3 deposition. A comparison of the coupled stomatal A_{net}–g_{sto} model with the multiplicative g_{sto} model within the DO_3SE framework was made in Pande et al. (2024), and it showed that the A_{net}–g_{sto} model performed equally well, if not better, when used to develop O_3 dose–response relationships for European wheat. This provides evidence of the suitability of the new photosynthesis-based g_{sto} model in DO_3SE.

In this study, we describe the development of a new DO_3SE-Crop model which builds on the modified stomatal deposition component of the DO_3SE model (Pande et al., 2024) so that both CO_2 uptake for carbon assimilation and O_3 uptake via the stomata can be modelled consistently. Further, we have incorporated the UK JULES-crop model (Osborne et al., 2015) to allocate assimilated carbon to plant components (roots, leaves, stems, and harvest organs) according to crop development stage. We also take account of the modifying effect of O_3 on instantaneous A_{net} as well as accumulated A_{net} via O_3 effects on the onset and rate of leaf senescence and timing of crop maturity through incorporation of algorithms developed by Ewert and Porter (2000). The UK JULES-crop model is used since this is the UK land surface exchange scheme in the UK Earth System Model (UKESM) (Osborne et al., 2015) which has recently been developed to include exchange and impact of trace gases (including O_3) along with other biogeochemical cycling between the atmosphere and the land surface (Leung et al., 2020). This would in the future allow comparison of the UK JULES-crop model, which uses O_3 mechanisms that modify instantaneous A_{net} to mimic changes in yield consistent with flux–response relationships (Sitch et al., 2007), with the alternative O_3 damage mechanisms used within DO_3SE-Crop.

Here, we calibrate and evaluate the DO_3SE-Crop model using an experimental FACE dataset collected in Xiaoji, China. This allows us to investigate the ability of the model to simulate O_3 damage for a comparable agro-ecological region where crop productivity is severely threatened by both O_3 pollution and climate change. The key objectives of the paper are to assess the ability of DO_3SE-Crop to simulate (i) key phenological stages, (ii) the relationship between leaf-

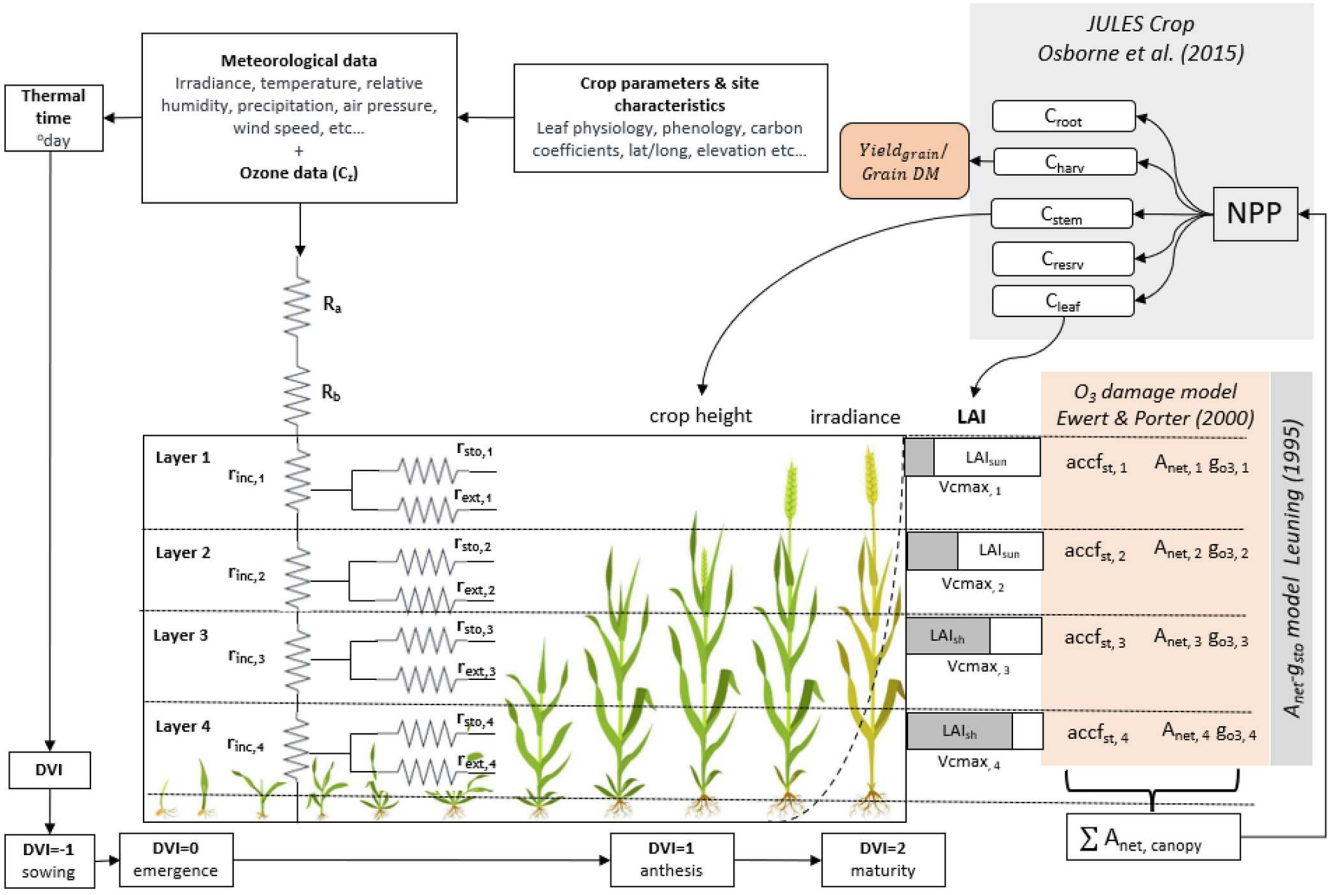

Figure 1. Schematic of the DO$_3$SE-Crop model.

level physiological variables and within-canopy O_3 concentrations, (iii) C allocation to different parts of the crop, and (iv) O_3-induced yield losses for tolerant and sensitive cultivars.

2 Methods

2.1 DO$_3$SE-Crop model

Here we describe the development of the DO$_3$SE-Crop model. In this study, version 4.39.16 of the DO$_3$SE-Crop model was used (Bland, 2024) for wheat (*Triticum aestivum*), which is widely considered to be one of the most sensitive staple crops to O_3 (Feng et al., 2018). The key components of DO$_3$SE-Crop are illustrated in Fig. 1. The model integrates meteorological data, crop parameters, and site characteristics to simulate the impact of O_3 on crop yield. Model inputs are irradiance, temperature, relative humidity, precipitation, air pressure, wind speed, and O_3 concentration at a reference height (C_z) to calculate atmospheric resistances (R_a) and boundary layer resistances (R_b) for O_3 deposition to the crop canopy. It further incorporates crop-specific parameters related to leaf physiology, phenology, and carbon coefficients, alongside site-specific data (latitude, longitude, and elevation) to simulate crop growth at stages from sowing to maturity, denoted by the development index (DVI). The canopy is divided into four vertical layers, each characterised by the sunlit leaf area index (LAI_{sun}) and the shaded (LAI_{sh}) leaf area index, which influence the photosynthetic capacity (V_{cmax}) and O_3 uptake in each layer. The model accounts for in-canopy resistance (r_{inc}) and external resistance (r_{ext}) in each layer, affecting the O_3 flux ($accf_{st}$) and its impact on net photosynthesis (A_{net}) and stomatal conductance (g_{O_3}). The A_{net}–g_{sto} relationship is modelled using the Leuning (1995) model. Damage from O_3 is estimated after Ewert and Porter (2000) for different canopy layers, which are aggregated to give the overall O_3 impact on canopy A_{net}, which is integrated according to the JULES-crop model (Osborne et al., 2015), which uses the daily accumulated canopy A_{net} to calculate the net primary productivity (NPP). The NPP is then distributed as carbon to various parts of the crop (roots (C_{root}), stems (C_{stem}), leaves (C_{leaf}), harvestable organs (C_{harv})). The C_{harv} provides the yield and grain dry matter, C_{leaf} provides the LAI, and C_{stem} provides the crop height. The DO$_3$SE-Crop model requires hourly input meteorological and O_3 concentration data which are used to

produce output on either an hourly (i.e. leaf physiology and short-term O_3 damage variables) or daily (i.e. phenology, soil moisture, long-term O_3 damage, C allocation, biomass, and yield variables) time step.

2.2 DO_3SE-Crop phenology

The DO_3SE-Crop model uses thermal time to define the rate of crop development in relation to the timing of three key developmental stages, TT_{emr} (the period from sowing to emergence), TT_{veg} (the period of emergence to start of grain filling), and TT_{rep} (the period from the start of grain filling to maturity), based on the method of Osborne et al. (2015). Thermal time is calculated by accumulating an effective temperature (T_{eff}) using base (T_b), optimum (T_o), and maximum (T_m) cardinal temperatures as shown in Eq. (1):

$$T_{eff} = \begin{cases} 0 & \text{for } T_{air} < T_b \\ T_{air} - T_b & \text{for } T_b \le T_{air} \le T_0 \\ (T_0 - T_b)\left(1 - \frac{T_{air}-T_0}{T_m-T_0}\right) & \text{for } T_0 < T_{air} < T_m \\ 0 & \text{for } T_{air} \ge T_m \end{cases}, \quad (1)$$

where T_{air} is the surface air temperature in °C, and T_{eff} is at a maximum when $T_{air} = T_o$; this point denotes the highest developmental rate. T_{eff} declines as the temperature falls or rises above T_o, with a linear decrease in crop development. T_{eff} is zero, i.e. no development, when T_{air} falls below or rises above T_b and T_m, respectively; i.e. $T_m \le T_{air} < T_b$. During the sowing to emergence phase, development is dependent on T_b, whereas during the vegetative and reproductive phase, development depends on T_m or T_o.

Winter wheat requires vernalisation (a period of exposure to low temperature during germination to accelerate flowering). Vernalisation alters the length of TT_{veg} and hence flowering initiation, with subsequent effects on later growth stages such as heading. Vernalisation occurs when the minimum (VT_{min}) and maximum (VT_{max}) daily temperature is less than 15 and 30 °C, respectively (Zheng et al., 2015). Accumulated vernalised days (V_{dd}) are calculated as the sum of vernalised and devernalised days from emergence to the start of anthesis (Zheng et al., 2015) as shown in Eq. (2):

$$V_{dd} = \sum (V - V_d), \quad (2)$$

where $V = \left(1.4 - 0.778 \times T_{air}\,,\, 0.5 + 13.44 \frac{T_{air}}{(T_{max}-T_{min}+3)^2}\right)$ for $VT_{max} < 30$ °C and $VT_{min} < 15$ °C, $V_d = \left(\min\left(0.5\,(T_{max} - 30)\,,\, V_{prev}\right)\right.$ for $VT_{max} > 30$ °C, and $V_{dd} < 10$ d.

The vernalisation factor (VF) decreases from 1 to 0 as (V_{dd}) increases. VF depends on a cultivar-specific vernalisation coefficient (PIV) as described by Eq. (3):

$$VF = 1 - (0.0054545 \times PIV + 0.0003) \times (50 - V_{dd}). \quad (3)$$

Photoperiod (PP) or day length also affects the occurrence and timing of the flowering stage and is calculated according to latitude using standard solar geometry to estimate day length (Jones, 1992). The photoperiod factor (PF) represents the sensitivity to PP, which decreases from 1 to 0 as the photoperiod shortens and is estimated according to a cultivar-specific photoperiod coefficient (PID) after Tao et al. (2012) as described in Eq. (4):

$$PF = 1 - \left[\left(\frac{PID}{10\,000}\right) \times (20 - PP)^2\right]. \quad (4)$$

Crop development is related to the development index (DVI) after Osborne et al. (2015), which takes values of -1 upon sowing, 0 on emergence, 1 at anthesis, and 2 at crop maturity. The DO_3SE-Crop model DVI equations have been modified from Osborne et al. (2015) to take account of the photoperiod and vernalisation for winter wheat (see Eq. 5); for spring wheat these factors are omitted:

$$\begin{aligned} &-1 \le DVI < 0 \quad \text{for} \quad TT_{eff} < TT_{emr} \\ &0 \le DVI < 1 \quad \text{for} \quad TT_{emr} \le TT_{eff} \times VF \times PF < TT_{veg} \\ &1 \le DVI \le 2 \quad \text{for} \quad TT_{veg} \le TT_{eff} \le TT_{rep}. \end{aligned} \quad (5)$$

DO_3SE-Crop allows for any number of representative leaf populations (pop) and canopy layers (n) to be defined over the course of the crop growing season by dividing leaf populations as they emerge evenly across the canopy layers defined by LAI. In this study, we used a single leaf population and four canopy layers (i.e. pop $= 1$; $n = 4$) for simplicity. The crop sowing is assumed to be at DVI $= -1$ (start of TT_{emr}) and emergence at DVI $= 0$ (start of TT_{veg}). The flag leaf is assumed to develop at DVI $= 1$, at the commencement of TT_{rep}, marking the initiation of anthesis (A_{start} flowering) and flag leaf emergence, which typically occurs 4–5 d prior to the onset of anthesis and is further divided into expanding and senescing leaf periods (i.e. tl_{ep} and tl_{se}) with a default ratio of 0.67 to 0.33 for each of these periods. Maturity is assumed at DVI =2, at the end of TT_{rep}. The model allows estimation of the POD_y metric by accumulating stomatal O_3 flux from the start of anthesis to maturity. The total canopy leaf life span (TT_{leaf}) of the crop is distributed over the DVI between 0 and 2. The total lifespan (T_l) covers the full period from sowing to maturity, corresponding to DVI between -1 and 2. The relationship between these different variables is described in Fig. 2.

2.3 DO_3SE-Crop leaf-level physiology

Key leaf-level physiological variables of the DO_3SE-Crop model are A_{net} and g_{sto}. Net photosynthesis is simulated using the biochemical photosynthesis-based model initially developed by Farquhar et al. (1980) and since modified by Sharkey et al. (2007). The coupled A_{net}–g_{sto} model of Leuning (1995) is used to estimate g_{sto} from A_{net}, which means that g_{sto} is regulated by the demand of CO_2 for A_{net} on consideration of environmental conditions and crop physiology. Ozone stress, causing both instantaneous effects on A_{net} and long-term effects on A_{net} via leaf senescence, is simulated based on algorithms developed by Ewert and Porter (2000).

2.3.1 Leaf net photosynthesis (A_{net})

The A_{net} model assumes that photosynthesis is constrained depending on prevailing environmental conditions according to three main mechanisms: rubisco activity (A_c); ribulose-1,5-bisphosphate (RuBP) regeneration, which is constrained by the speed of electron transport (A_j); and the low rate of transfer of photosynthetic products (most frequently triose phosphate consumption) (A_p) (Sharkey et al., 2007) and by soil water stress (f_{PAW}). The algorithm for A_c, which is based on Medlyn et al. (2002) and modified in DO$_3$SE-Crop to include the O_3 damage functions, is given in Eq. (6):

$$A_c = V_{cmax} \times f_{PAW} \times \frac{(C_i - \Gamma^*) \times fO_{3,s}(d) \times f_{LS}}{C_i + K_c\left(1 + \frac{O_i}{K_o}\right)}, \quad (6)$$

where V_{cmax} (μmol CO$_2$ m^{-2} s^{-1}) is the maximum carboxylation capacity at 25 °C, C_i (μmol mol^{-1}) and O_i (mmol mol^{-1}) are the intercellular CO_2 and O_2 partial pressures, K_c (μmol mol^{-1}) and K_0 (mmol mol^{-1}) are the rubisco Michaelis–Menten constants for CO_2 and O_2, Γ^* (μmol mol^{-1}) is the CO_2 compensation point in the absence of respiration, $fO_{3,s}(d)$ is the factor that accounts for the cumulative stomatal O_3 flux effect on V_{cmax} over the course of a day, and f_{LS} is the factor that accounts for the cumulative stomatal O_3 flux effect over the course of a leaf life span on leaf senescence. Section 2.3.2 gives a full description of the methods used to estimate O_3 damage. The f_{PAW} factor is calculated by Eq. (7):

$$f_{PAW} = 1 \quad \text{for } PAW_t \le PAW \le 100\,\%,$$
$$f_{PAW} = 1 + \{\frac{PAW - PAW_t}{PAW_t}\} \quad \text{for } PAW \le PAW_t. \quad (7)$$

PAW is the amount of water in the soil (in % terms) which is available to the plant estimated according to the DO$_3$SE models' single-soil-layer bucket model (Büker et al., 2012). At PA = 100 % the soil is at field capacity; at PAW = 0, % the soil is at wilting point. PAW_t is the threshold PAW, above which it is assumed there is no constraint on A_c, defined as 50 % after LRTAP (2017). Only once PAW < PAW_t will soil water begin to limit g_{sto} and hence stomatal O_3 flux.

The constraint on photosynthesis due to the rate of electron transport A_j is described in Eq. (8):

$$A_j = J \times \frac{C_i - \Gamma^*}{a \times C_i + b \times \Gamma^*}, \quad (8)$$

where J is the electron transport rate (μmol CO$_2$ m^{-2} s^{-1}), and the parameters a and b denote the electron requirements for the formation of NADPH and ATP, respectively (Sharkey et al., 2007)

Finally, the photosynthesis limitation due to the low rate of transfer of photosynthetic products A_p (μmol CO$_2$ m^{-2} s^{-1}) is given in Eq. (9):

$$A_p = 0.5 \times V_{cmax}. \quad (9)$$

The leaf net photosynthesis (A_{net}) in μmol CO$_2$ m^{-2} s^{-1} is calculated by Eq. (10):

$$A_{net} = \left(A_c, A_j, A_p\right) - R_d, \quad (10)$$

where leaf dark respiration (R_d) in μmol CO$_2$ m^{-2} s^{-1} is calculated as $V c_{max} \times R_{dcoeff}$, where R_{dcoeff} is the leaf dark respiration coefficient initially set equal to 0.015 after Clark et al. (2011) – a value provided for C_3 grasses.

2.3.2 Short- and long-term O_3 damage to A_c

The short-term impact of O_3 on A_c is calculated according to the $fO_{3,s}(d)$ factor (between 0 and 1), which allows for an instantaneous effect of O_3 on photosynthesis when stomatal O_3 flux (f_{st}), in nmol O$_3$ m^{-2} s^{-1} and calculated as described later in Sect. 1.2.3, overwhelms detoxification and repair mechanisms (Betzelberger et al., 2012; Y. Feng et al., 2022) and is estimated following Ewert and Porter (2000). Here, $f_{O_{3,s}}(h)$ represents the relationship between f_{st} and a potential decrease in A_c calculated for every hour of the day by Eq. (11):

$$f_{O_{3,s}}(h) = 1; \quad \text{for } f_{st} \le \frac{\gamma 1}{\gamma 2}$$
$$f_{O_{3,s}}(h) = 1 + \gamma 1 - \gamma 2 \times f_{st}$$
$$\text{for } \frac{\gamma 1}{\gamma 2} < f_{st} < \frac{1+\gamma 1}{\gamma 2}$$
$$f_{O_{3,s}}(h) = 0; \quad \text{for } f_{st} \ge \frac{1+\gamma 1}{\gamma 2}, \quad (11)$$

where $\gamma 1$ (dimensionless) and $\gamma 2$ (nmol O$_3$ m^{-2} s^{-1})$^{-1}$ are both short-term O_3 damage coefficients, with $\gamma 1$ representing the O_3 detoxification threshold below which no damage occurs to the photosynthetic system and $\gamma 2$ determines the effect of f_{st} on A_c once this detoxification threshold is exceeded; $fO_{3,s}(d)$ and $fO_{3,s}(d-1)$ (i.e. $fO_{3,s}(d)$ at the end of the previous day) are calculated by Eq. (12),

$$f_{O_{3,s}}(d) = f_{O_{3,s}}(h) \times r_{O_{3,s}};$$
$$\text{for PAR} \le 50\,\text{W m}^{-2}$$
$$f_{O_{3,s}}(d) = f_{O_{3,s}}(h) \times f_{O_{3,s}}(d-1)$$
$$\text{for PAR} > 50\,\text{W m}^{-2}, \quad (12)$$

where $r_{O_{3,s}}$ (dimensionless) represents incomplete recovery from O_3 overnight, which depends on leaf age according to Eq. (13),

$$r_{O_{3,s}} = f_{O_{3,s}}(d-1) + \left(1 - f_{O_{3,s}}(d-1)\right) \times f_{LA}. \quad (13)$$

The long-term impact of O_3 on V_{cmax} represented by the f_{Ls} term represents the longer-term accumulation of stomatal O_3 flux (acc_{fst}), causing degradation to the rubisco enzyme, which triggers early and enhanced senescence of mature leaves (Gelang et al., 2000; Osborne et al., 2019). The

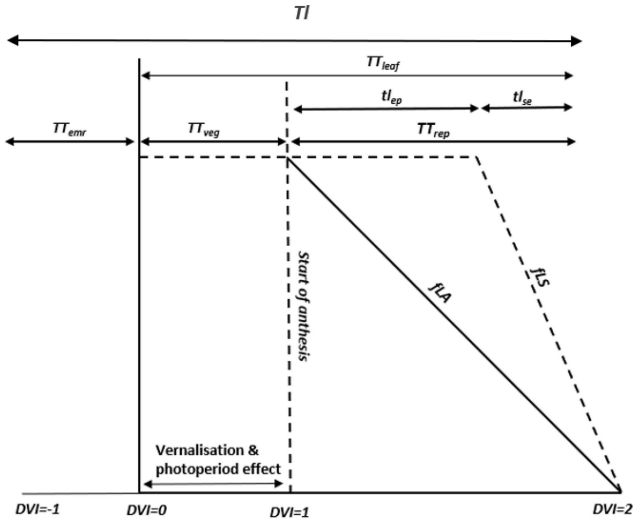

Figure 2. The division of thermal-time-defined periods (TT_{emr}, TT_{veg}, TT_{rep}, and TT_{leaf} and the relationship with f_{LA} and f_{Ls}) for the canopy, as represented in this study by a single leaf population.

acc_{fst} term is accumulated from 200 °C days before anthesis until maturity to be consistent with LRTAP (2017), which defines this as the O_3-sensitive period for wheat. The simulation of f_{Ls} (and f_{LA} used in the short-term O_3 effect) is related to thermal-time-defined periods over the course of a leaf population life span TT_{leaf} as described in Fig. 2.

The O_3 effect on f_{Ls} is first simulated by estimating a weighted accumulated fst ($fO3_l$) modified from Ewert and Porter (2000) by Eq. (14):

$$fO3_l = 1 - \max(\min(\gamma 3 \times (\mathrm{acc_{fst}} - \mathrm{CLsO3}), 1), 0), \quad (14)$$

where $\gamma 3$ determines the occurrence of senescence once a critical cumulative stomatal O_3 flux CLsO3 (in mmol m^{-2}) has been exceeded. The rate of senescence is determined by $\gamma 4$, which determines the onset of senescence, and $\gamma 5$, which determines maturity as described in Eq. (15):

$$\begin{aligned} tl_{\mathrm{ep_{O_3}}} &= tl_{\mathrm{ep}} \times (1 - ((1 - fO3_l) \times \gamma 4)) \\ tl_{\mathrm{se_{O_3}}} &= tl_{\mathrm{se}} \times (1 - ((1 - fO3_l) \times \gamma 5)) + zc \\ zc &= tl_{\mathrm{ep}} - tl_{\mathrm{ep_{O_3}}}, \end{aligned} \quad (15)$$

where tl_{ep} is the thermal time accumulated by a leaf (LTT) in °C days between a fully expanded leaf and the start of leaf senescence, $tl_{ep_{O_3}}$ is tl_{ep} with an O_3 effect which may bring senescence earlier, tl_{se} is the LTT in °C days between the onset of senescence and maturity, and $tl_{se_{O_3}}$ is tl_{se} with an O_3 effect which may bring maturity earlier. f_{Ls} is estimated by Eq. (16):

$$\begin{aligned} f_{\mathrm{Ls}} &= 1; && \text{for LTT} \le TT_{\mathrm{veg}} + tl_{\mathrm{ep}} \\ f_{\mathrm{Ls}} &= 1 - \frac{\mathrm{LTT} - TT_{\mathrm{veg}} - tl_{\mathrm{ep_{O_3}}}}{tl_{\mathrm{se_{O_3}}}}; \\ & \quad \text{for } TT_{\mathrm{veg}} + tl_{\mathrm{ep}} < \mathrm{LTT} < TT_{\mathrm{leaf}} \\ f_{\mathrm{Ls}} &= 0; && \text{for LTT} \ge TT_{\mathrm{leaf}}. \end{aligned} \quad (16)$$

2.3.3 Stomatal conductance (g_{sto})

The coupled photosynthesis–stomatal-conductance (A_{net}–g_{sto}) model based on Leuning (1995) and modified for vapour pressure deficit (VPD) is used to estimate g_{CO_2} and stomatal conductance to CO_2 in µmol CO_2 m^{-2} s^{-1} as described in Eq. (17),

$$g_{\mathrm{CO_2}} = [f_{\min} + m \times A_{\mathrm{net}} \times f_{\mathrm{VPD}}/(c_{\mathrm{s}} - \Gamma)], \quad (17)$$

where f_{min} (µmol m^{-2} s^{-1}) is the minimum daytime g_{CO_2} (Leuning, 1990). The parameter m (dimensionless) is the composite sensitivity of g_{CO_2} to assimilation rate and vapour pressure deficit (VPD), with the relationship between VPD and relative stomatal conductance (f_{VPD}) estimated by Eq. (18),

$$f_{\mathrm{VPD}} = \left(1 + \left(\frac{\mathrm{VPD}}{\mathrm{VPDo}}\right)^{8}\right)^{-1}, \quad (18)$$

where VPD_0 is an empirical parameter, defined using boundary line analysis, describing the variation in relative stomatal conductance with VPD (Danielsson et al., 2003; Pleijel et al., 2007). c_s (mmol mol^{-1}) is the external CO_2 concentration at the leaf surface and is calculated from the external CO_2 concentration at the upper surface of the leaf boundary layer c_a (mmol mol^{-1}) so that $c_{\mathrm{s}} = c_a - \left(\frac{A_{\mathrm{net}}}{g_{\mathrm{bCO_2}}}\right)$ after Masutomi (2023), where g_{bCO_2} is the boundary layer conductance to CO_2 (in mol m^{-2} s^{-1}), and conversion factors for gases and heat across the boundary layer are given in Sect. S1a.

Finally, g_{CO_2} is converted to g_{O_3} in mmol O_3 m^{-2} s^{-1} by dividing by 1000 and using the conversion factor 0.96, which assumes that the ratio of the diffusivities of gases in air is equal to the inverse of the square root of the ratio of molecular weights (as described in Campbell and Norman, 1998); see also Sect. S1b).

2.3.4 Stomatal ozone flux (f_{st})

Stomatal [O_3] flux (f_{st} in nmol m^{-2} s^{-1}) is calculated after the method described in the UNECE mapping manual (LRTAP, 2017) described in Eq. (19):

$$f_{\mathrm{st}} = C_{\mathrm{l}} \times g_{\mathrm{O_3 m/s}} \times \frac{r_{\mathrm{c}}}{r_{\mathrm{b,O_3}} + r_{\mathrm{c}}}, \quad (19)$$

where C_l is the [O_3] at the upper surface of the laminar layer of a leaf (nmol O_3 m^{-3}). Ozone concentration in ppb can be

converted to nmol m^{-3} by multiplying O_3 in ppb by $P/(R \times T_{air,k})$, where P is the atmospheric pressure (1.013×10^5 in Pascal), R is the universal gas constant (8.31447 J mol K^{-1}), and $T_{air,k}$ is surface air temperature in °K. To convert g_{O_3} (mol O_3 m^{-2} s^{-1}) to $g_{O_3 m/s}$ (m s^{-1}) we assume a standard temperature (20 °C) and P divided by 41 to give the conductance value in m s^{-1}. The $r_c/(r_{b,O_3} + r_c)$ term represents the O_3 deposition rate to the leaf through resistances r_b (the quasi-laminar resistance (s m^{-1})) and r_c (the leaf surface resistance (s m^{-1})), which allow for both stomatal and non-stomatal deposition to the leaf surface. r_c is $1/(g_{O_3 m/s} + g_{ext})$, where g_{ext} is 1/2500 (s m^{-1}). r_{b,O_3} is estimated by Eq. (20):

$$r_{b,O_3} = 1.3 \times 150 \times \sqrt{\frac{L}{u_1}}, \quad (20)$$

where the factor 1.3 accounts for the differences in diffusivity between heat and O_3 (see Sect. S1a), L is the cross-wind leaf dimension (m), and u_1 is the wind speed (m s^{-1}) at the top of the leaf laminar boundary layer. The leaf boundary layer resistance to CO_2 is estimated using a value of 1.24 for the difference between heat and CO_2 in place of the 1.3 value for O_3 (Campbell and Norman, 1998).

2.4 DO$_3$SE-Crop canopy

The DO$_3$SE-Crop model uses a multi-layer approach to scale from leaf to the canopy. We assume that wind, irradiance, [O_3] concentration, and leaf nitrogen content are the key environmental conditions which change with the cumulative canopy leaf area index (LAI) and influence leaf physiology and therefore canopy layer estimates of A_{net}, g_{O_3}, and g_{ext}; other environmental variables (e.g. T_{air} and VPD) are assumed to remain constant over the canopy.

2.4.1 Canopy irradiance

Changes in irradiance through the canopy are described as sunlit and shaded canopy fractions and the associated quantity of direct and diffuse photosynthetically active radiation (PAR, W m^{-2}); these are estimated according to increasing levels of cumulative LAI using the methods of (de Pury and Farquhar, 1997); full details are given in the Sect. S2. Application of this method requires the canopy to be divided into layers of equal LAI, including both green LAI (LAI_G) and brown (LAI_B) LAI.

PAR absorbed per unit leaf area is divided into PAR_{dir} and PAR_{diff}, which also includes scattered (re-reflected by the canopy) beam calculated by

$$PAR_{dir}(LAI) = (1 - \rho_{cb}(\beta))\, k_b{}'\, I_b(0) \exp(-k'_b LAI), \quad (21)$$

$$PAR_{diff}(LAI) = (1 - \rho_{cd})\, k_d\, I_d(0) \exp(-k_d LAI), \quad (22)$$

where PAR_{dir} is the absorbed beam plus scattered beam PAR (photosynthetically active radiation) per unit leaf area, PAR_{diff} is the absorbed diffuse plus scattered diffuse PAR per unit leaf area, ρ_{cb} is the canopy reflection coefficient for beam PAR, ρ_{cd} is the canopy reflection coefficient for diffuse PAR, k'_b is the beam and scattered beam PAR extinction coefficient, k'_d is the diffuse and scattered diffuse PAR extinction coefficient, β is the solar elevation above the horizontal plane of the Earth's surface, $I_b(0)$ is beam PAR per unit ground area at the top of the canopy, and $I_d(0)$ is diffuse PAR per unit ground area at the top of the canopy.

Estimates of the LAI fractions of sunlit (LAI_{sun}) and shaded (LAI_{sh}) parts of each canopy layer (i) are made by Eqs. (23) and (24):

$$LAI_{sun,i} = \left[1 - \exp\left(-0.5 \times \frac{LAIi}{\sin\beta}\right)\right] \times 2\sin\beta, \quad (23)$$

where β is the solar elevation angle (see Sect. S3), and

$$LAI_{sh,i} = LAI_i - LAI_{sun,i}. \quad (24)$$

The DO$_3$SE-Crop model simulates LAI as part of the crop growth model, and LAI is assumed to be evenly distributed across all layers (see Sect. 1.4.2 and Eq. 43).

Therefore, PAR for the sunlit part of each layer (PAR_{sun}) can be described as

$$\int_{LAI_i}^{LAI_n} PAR_{sun} = \int_{LAI_i}^{LAI_n} (LAI_{sun,i}) \times (PAR_{sh} + PAR_{bsun}(\beta))\, dLAI,$$

where PAR_{sh} is absorbed PAR by shaded leaves per unit leaf area; PAR_{bsun} is beam PAR absorbed by sunlit leaves per unit leaf area; and $\int_{LAI_i}^{LAi_n} PAR_{dir}$ can be written as $(1 - \rho cb(\beta)) \times k_b{}' \times Ib \times [\exp(-k_b{}' LAI_i) - \exp(-k_b{}' LAI_n)]$ and $PAR_{bsun}(\beta) = (1 - \sigma)\, I_b(0)\, \frac{Cos_{\alpha_1}}{Sin\beta}$, where α_1 is angle of irradiance beam on the leaf normal and σ is the leaf scattering coefficient for PAR.

Similarly, PAR for the shaded part of each layer (PAR_{sun}) can be described as

$$\int_{LAI_i}^{LAI_n} PAR_{sh} = \int_{LAI_i}^{LAI_n} (LAI_{sh,i}) \times (PAR_{diff} + PAR_{bsun}) dLAI,$$

where $\int_{LAi_i}^{LAi_n} (PAR_{diff}(LAI)$ can be written as $(1 - \rho_{cd}) \times k_b{}' \times Ib \times [\exp(-k'_d LAI_i) - \exp(-k'_d LAI_n)] dL$, $\int_{LAi_i}^{LAi_n} PAR_{bs}(LAI)$ is $I_b(0)\,[PAR_{dir} - (1 - \sigma)\, k_b \times [\exp(-k_b LAI_i) - \exp(-k_b LAI_n)]$, and $PAR_{bs}(LAI)$ is absorbed scattered beam PAR per unit leaf area.

2.4.2 Canopy [O_3] concentration

O_3 concentration will vary as a function of O_3 loss to the canopy (i.e. deposition via the stomates and external plant parts) and O_3 replacement from ambient air concentrations above the canopy. Limited data have been collected showing how O_3 concentrations vary with canopy depth in semi-natural communities (Jaggi et al., 2006). These data suggest

that a minimum, bottom of canopy O_3 concentration (C_{zb}) is about 0.2 times that at the top of the canopy (C_{zh}) and that the O_3 concentration difference within the canopy is closely related to the LAI of the canopy layers.

Since each canopy layer can be assumed to be a parallel sink, the O_3 flux to a layer depends on the conductance (inverse of resistance) of that layer and the O_3 concentration at the top of the layer (C_i; with C_0 being C_{zh} (i.e. the O_3 concentration at height C_h, the top of the canopy)); we follow and generalise the work of Waggoner (1971) by separating the canopy into nL leaf layers. We calculate the O_3 concentration for each layer, C_i, from O_3 intake, I_i, by

$$C_i = r_{c,i} I_i, \tag{25}$$

with $r_{c,i}$ the leaf surface resistance to O_3 for layer i. I_i is calculated as the solution to a system of linear equations. The in-canopy aerodynamic resistance for layer i is described in terms of $r_{c,i}$, I_i, and the resistances of the bulk air among the leaves (R_i). Assuming a uniform O_3 concentration C_0 above the canopy, we use generalised equations from Waggoner (1971) to calculate the difference in O_3 concentration between the exterior air and the leaf interior. For the top layer, this difference is C_0 minus 0, while for each lower layer, the difference decreases progressively depending on the resistances and fluxes within the canopy. This O_3 concentration difference is calculated by

$$C_0 = R_i \sum_{j=1}^{\mathrm{nL}} I_j + r_{c,1} I_1 \tag{26}$$

for the top canopy layer,

$$0 = R_i \sum_{j=i}^{\mathrm{nL}} I_j + r_{c,i} I_i - r_{c,i-1} I_{i-1} \tag{27}$$

for each canopy layer i between the top layer and the bottom layer, and

$$0 = R_{\mathrm{nL}+1} I_{\mathrm{nL}+1} - r_{c,\mathrm{nL}} I_{\mathrm{nL}} \tag{28}$$

for the bottom layer of the canopy between the lowest leaf layer and the ground. These can also be written into the matrix form

$$\begin{pmatrix} r_{c,1}+R_1 & R_1 & R_1 & \cdots & R_1 \\ -r_{c,1} & r_{c,2}+R_2 & R_2 & \cdots & R_2 \\ 0 & -r_{c,2} & r_{c,3}+R_3 & \cdots & R_3 \\ \vdots & \vdots & \vdots & \ddots & \vdots \\ 0 & 0 & 0 & \vdots & R_{nL+\_1} \end{pmatrix} \begin{pmatrix} I_1 \\ I_2 \\ I_3 \\ \vdots \\ I_{nL+1} \end{pmatrix} = \begin{pmatrix} C_0 \\ 0 \\ 0 \\ \vdots \\ 0 \end{pmatrix}, \tag{29}$$

which can be numerically solved for I_x when $r_{c,1} \neq 0$ and $R_1 \neq 0$.

Resistances for each layer are calculated as described in the Supplement (Sect. S5) using standard DO_3SE deposition modelling methods (Emberson et al., 2000, 2001).

2.4.3 Canopy maximum carboxylation capacity (V_{cmax})

We allow for an exponential decrease in leaf N with canopy depth, which will influence both the photosynthetic capacity (V_{cmax}) and dark respiration (R_{dc}). Photosynthetic capacity at each canopy layer i is calculated by Eq. (30):

$$V_{\mathrm{cmax},i} = n_e \times n_0 \times e^{-kN\left(\frac{\mathrm{LAI}i}{\mathrm{LAI}}\right)}, \tag{30}$$

where n_e (mol CO_2 m^{-2} s^{-1} kg C (kg N)$^{-1}$) is a constant relating leaf nitrogen to rubisco carboxylation capacity, n_0 (kg N[kg C]$^{-1}$) is the leaf N concentration at the top of the canopy, and kN is a nitrogen profile coefficient initially set at 0.78 after (Clark et al., 2011). The model assumes non-limiting conditions for soil nitrogen, in accordance with the experimental data.

2.4.4 Canopy photosynthesis ($Anet_c$)

Net canopy photosynthesis ($Anet_c$) determines the amount of C assimilated by the entire canopy that can subsequently be allocated to different plant parts (i.e. less than the C respired for plant growth and maintenance; see Sect. 1.4.1); the amount of C assimilation will ultimately determine whole-plant biomass. The net photosynthesis for each canopy layer ($Anet_i$) is calculated according to the LAI fraction of that layer that is sunlit ($LAI_{sun,i}$) and shaded ($LAI_{sh,i}$) within the layer (i), multiplied by the net photosynthesis of the sunlit ($Anet_{sun,i,j}$) and shaded leaf ($Anet_{sh,i,j}$), respectively, described by Eqs. (31) and (32):

$$\mathrm{Anet}_i = \mathrm{LAI}_{\mathrm{sun},i} \times \mathrm{Anet}_{\mathrm{sun},i} + \mathrm{LAI}_{\mathrm{sh},i} \times \mathrm{Anet}_{\mathrm{sh},i}, \tag{31}$$

with $Anet_c$ calculated by

$$\mathrm{Anet_c} = \sum\nolimits_{i=1}^{n} \mathrm{Anet}_i. \tag{32}$$

$Anet_c$ is converted from μmol CO_2 m^{-2} s^{-1} to kg C m^{-2} d^{-1} by multiplying by 3600 (converting from seconds to hours), multiplying by 1.2 (representing the kg of C per mol), and summing each hourly $Anet_c$ over the course of a day. This $Anet_c$ is used in the Eq. (37).

2.4.5 Canopy stomatal conductance (g_{O_3c})

Similarly, canopy layer (i) stomatal conductance to O_3 (g_{O_3i}) is converted from g_{CO_2} by assuming a diffusivity ratio of 0.96 to convert from CO_2 to O_3 and is calculated by Eq. (33) with whole-canopy stomatal conductance calculated by Eq. (34):

$$g_{\mathrm{O_3}i} = \mathrm{LAI}_{\mathrm{sun},i} \times g_{\mathrm{O_3sun},i} + \mathrm{LAI}_{\mathrm{sh},i} \times g_{\mathrm{O_3sh},i}, \tag{33}$$

$$g_{O_{3c}} = \sum_{i=1}^{n} g_{O_{3i}}. \quad (34)$$

This is converted from $g_{O_{3i}}$ in Eq. (33) by dividing the conductance value in mmol m^{-1} s^{-1} by 41 000 (assuming standard temperature (20 °C) and air pressure (1.013×10^5 Pa)) to give conductance in m s^{-1}.

2.5 Crop biomass, LAI, height, and yield variables

The following section describes how to estimate crop biomass, important canopy characteristics (LAI and crop height (h)), and yield variables from accumulated calculations of Anet_c over the course of the growing season following (Osborne et al., 2015).

2.5.1 Crop biomass (NPP and GPP)

The simulation of crop growth requires an estimate of the net primary productivity (NPP) which is calculated at the end of each day and summed over the growing season. Carbon is assumed to be allocated to five key crop components: root, leaf, stem, harvest, and reserve pools (Osborne et al., 2015). This carbon allocation is ultimately used to simulate leaf area index (LAI), canopy height (h), biomass, harvest index, and yield at the end of each day throughout the growing season.

NPP (kg C m^{-2} d^{-1}) is accumulated throughout the day using the JULES-crop approach to model crop growth (Osborne et al., 2015) described in Eq. (35),

$$\text{NPP} = \text{GPP} - R_p, \quad (35)$$

where GPP is the gross primary productivity (kg C m^{-2} d^{-1}) and R_p is plant respiration divided into maintenance (R_{pm}) and growth (R_{pg}) respiration (kg C m^{-2} d^{-1}) (Clark et al., 2011), where $R_p = R_{pm} + R_{pg}$ and where R_{pg} is assumed to be a fixed fraction of the NPP as shown in Eq. (36),

$$R_{pg} = R_{gcoeff}(\text{GPP} - R_{pm}), \quad (36)$$

where R_{gcoeff} is the growth respiration coefficient which was initially set to 0.25 based on the value for all PFTs (i.e. forests and grasses including crops) in Clark et al. (2011). GPP is calculated by Eq. (37):

$$\text{GPP} = \text{Anet}_c + f_{PAW} R_{dc}, \quad (37)$$

where Anet_c is net canopy photosynthesis (see Eq. 28) and $f_{PAW} R_{dc}$ is the soil-moisture modified canopy dark respiration (kg C m^{-2} d^{-1}), where $R_{dc} = V_{cmax,i} \times R_{dcoeff}$, with R_{dcoeff} initially assumed to be 0.015 based on Clark et al. (2011); $V_{cmax,i}$ is the maximum carboxylation efficiency for each canopy layer i, which decreases from the top to bottom of the canopy (see Eq. 30); and f_{PAW} is calculated in Eq. (7).

Leaf maintenance respiration (R_{pm}) is assumed to be equivalent to the soil moisture modified canopy dark respiration, while root and stem respiration are assumed to be independent of soil moisture but to have the same dependencies on C content. We assume a fixed relationship between C and N contents of these organs so that R_{pm} can be estimated by Eq. (38):

$$R_{pm} = R_{dc} \times \left(f_{sw} + \left(\frac{C_{root} + C_{stem}}{C_{leaf}} \right) \right). \quad (38)$$

The C accumulating as NPP each day is divided into five carbon pools, i.e. root (C_{root}), leaf (C_{leaf}), stem (C_{stem}), reserve (C_{resv}), and harvest (C_{harv}) (kg C m^{-2} d^{-1}), according to partition coefficients (see Eq. 39) allowing for accumulation of C in these pools over the course of the crop growth period:

$$\begin{aligned}
\frac{\text{dC_root}}{\text{d}t} &= p_{root}\text{NPP}, \\
\frac{\text{dC_leaf}}{\text{d}t} &= p_{leaf}\text{NPP}, \\
\frac{\text{dC_stem}}{\text{d}t} &= p_{stem}\text{NPP}\,(1-\tau), \\
\frac{\text{dC_harv}}{\text{d}t} &= p_{harv}\text{NPP}, \\
\frac{\text{dC}_{resv}}{\text{d}t} &= p_{stem}\text{NPP}, \tau,
\end{aligned} \quad (39)$$

where τ is the fraction of stem C that is partitioned into the reserve pool. $p_{root} p_{leaf}$, p_{stem}, and $p_{harv} = 1$. The partition coefficients are related to the crop development stage (DVI) and hence effective thermal time (TT_{eff}) since emergence. The partition coefficients are based on Osborne et al. (2015) and provided as a function of DVI using six parameters to continuously describe varying partition coefficients over the duration of the crop growing season. We use the same multinomial logistic as that described in Osborne et al. (2015) to define this function according to Eq. (40):

$$\begin{aligned}
p_{root} &= \frac{e^{\alpha_{root}+(\beta_{root}\,\text{DVI})}}{e^{\alpha_{root}+(\beta_{root}\,\text{DVI})} + e^{\alpha_{stem}+(\beta_{stem}\,\text{DVI})} + e^{\alpha_{leaf}+(\beta_{leaf}\,\text{DVI})} + 1}, \\
p_{stem} &= \frac{e^{\alpha_{stem}+(\beta_{stem}\,\text{DVI})}}{e^{\alpha_{root}+(\beta_{root}\,\text{DVI})} + e^{\alpha_{stem}+(\beta_{stem}\,\text{DVI})} + e^{\alpha_{leaf}+(\beta_{leaf}\,\text{DVI})} + 1}, \\
p_{leaf} &= \frac{e^{\alpha_{leaf}+(\beta_{leaf}\,\text{DVI})}}{e^{\alpha_{root}+(\beta_{root}\,\text{DVI})} + e^{\alpha_{stem}+(\beta_{stem}\,\text{DVI})} + e^{\alpha_{leaf}+(\beta_{leaf}\,\text{DVI})} + 1}, \\
p_{harv} &= \frac{1}{e^{\alpha_{root}+(\beta_{root}\,\text{DVI})} + e^{\alpha_{stem}+(\beta_{stem}\,\text{DVI})} + e^{\alpha_{leaf}+(\beta_{leaf}\,\text{DVI})} + 1},
\end{aligned} \quad (40)$$

where DVI is the development index, and α and β are partition parameters. These parameters describe the shape of the thermal-time varying partition coefficient for leaves, roots, and stems.

Once C is no longer partitioned to stems, C from the stem reserve pool will mobilise to the harvest pool at a rate of 10 % per day following Osborne et al. (2015) and described

by Eq. (41):

$$C_{\text{harv}} = C_{\text{harv}} + (0.1\,C_{\text{resv}})\; C_{\text{resv}} = 0.9\,C_{\text{resv}}\}$$
$$\text{for } p_{\text{stem}} < 0.01. \tag{41}$$

Total leaf C is divided between green leaf C ($C_{\text{leaf, green}}$) and brown leaf carbon ($C_{\text{leaf, brown}}$). Carbon from the $C_{\text{leaf, green}}$ will mobilise to the harvest pool at a rate of 5% per day after Osborne et al. (2015) and to the $C_{\text{leaf, brown}}$ at a rate of 24 % per day once $f_{\text{LS}} > 1$ as described in Eq. (42):

$$\{\mathrm{C_{harv}} = \mathrm{C_{harv}} + \left(0.05\,\mathrm{C_{leaf,green}}\right)\,\mathrm{C_{leaf,green}} = 0.86$$
$$\mathrm{C_{leaf}}\;\mathrm{C_{leaf}} = 0.86\mathrm{C_{leaf,\,green}} + 0.24\mathrm{C_{leaf,\,brown}}\}$$
$$\text{for } f_{\text{LS}} > 1. \tag{42}$$

2.5.2 Leaf area index (LAI) and stem height (h)

At the end of each day, the C content of the stem and leaf is used to estimate LAI by Eqs. (43) and (44):

$$\mathrm{LAI} = (\mathrm{C_{leaf}}\,/\,f_{\mathrm{c}}) \times \mathrm{SLA}, \tag{43}$$

$$\text{where } \mathrm{SLA} = \Upsilon\,(\mathrm{DVI} + 0.06)^{\delta}. \tag{44}$$

The values Υ and δ were determined by fitting the values to the paired values of DVI and specific leaf area (SLA). The value of f_{c} is 0.5 (unitless) and denotes the carbon fraction of dry matter.

The amount of C in the stem is used to calculate the crop height h in metres by Eq. (45):

$$h = k(C_{\text{stem}}/f_{\mathrm{c}})^{\lambda}, \tag{45}$$

where k and λ were determined by fitting the value C_{stem} and h.

2.5.3 Yield variables

According to Osborne et al. (2015) yield can be calculated from the C allocated to the harvest pool (C_{harv}) at the end of the growing season as described in Eq. (46):

$$\mathrm{Yield_{grain}} = \frac{(\mathrm{C_{harv}} \times (1/f_{\mathrm{c}}) \times D_w \times E_{\mathrm{g}})}{1000}, \tag{46}$$

where harvested C is converted to total biomass (using the conversion factor $f_{\mathrm{c}} = 0.5$), i.e. by multiplying the harvested C by $1/f_{\mathrm{c}}$ and then by 1/0.84 (D_w) to account for the grain moisture content (Mulvaney and Devkota, 2020). $\mathrm{C_{harv}}$ includes both chaff and grain; however, O_3 fumigation experimentalists tend to only include grain when calculating total crop yield at the end of the growing season, so we assume 15 % of the yield is chaff and include a grain-to-ear ratio, E_{g}, of 0.85. Dividing by 1000 converts yield from $\mathrm{kg\,C\,m^{-2}}$ to $\mathrm{g\,C\,m^{-2}}$, the unit most often used to describe experimental yield results.

Evaluation of the DO_3SE-Crop model uses a variety of growth dry matter (DM) metrics. Some of the most important metrics and their calculations are "straw DM", which is calculated as the sum of carbon allocated to $\mathrm{C_{stem}}$, $\mathrm{C_{leaf}}$, and $\mathrm{C_{resv}}$; "ear DM", which is calculated from $\mathrm{C_{harv}}$ excluding the moisture content (D_w) conversion; "grain DM", which is calculated from $\mathrm{C_{harv}}$ excluding both the moisture content (D_w) conversion and removing the chaff fraction conversion E_{g}; "above-ground DM", which is the straw DM plus the ear DM; "below-ground DM", which is converted from $\mathrm{C_{root}}$; and "harvest index", which is the grain DM divided by the above-ground DM. In all cases the f_{c} conversion factor is used to convert from, for example, $\mathrm{g\,C\,m^{-2}}$ to $\mathrm{g\,DM\,m^{-2}}$.

3 DO_3SE-Crop model calibration

3.1 Xiaoji China experimental dataset

The DO_3SE-Crop model was used to analyse the O_3-FACE (Free Air Concentration Enrichment) experimental data collected in Xiaoji, Jiangdu, Jiangsu Province, China. The wheat crop was grown in fully open-air field conditions for three consecutive growing seasons from 2007 to 2009. The dataset includes four modern cultivars of winter wheat (*Triticum aestivum* L.) grown under ambient (AA) and elevated (E) O_3, with the elevated treatment being, on average, 25 % above the ambient O_3 concentrations from early March/April to the end of May each year. The four cultivars were Yannong 19 (strong-gluten wheat, hereafter Y19), Yangmai 16 (medium-gluten wheat, hereafter Y16), Yangmai 15 (weak-gluten wheat, hereafter Y15), and Yangfumai 2 (weak-gluten wheat, hereafter Y2) (Zhu et al., 2011).

Soil water availability was sufficient for optimum wheat crop growth, so we assumed there was no soil moisture stress (Feng et al., 2012). Any data gaps were filled following the AgMIP-O_3 gap-filling protocol (see Sect. S4). For large O_3 data gaps (i.e. greater than 2 weeks) occurring outside the O_3 fumigation period, we used scaled WRF-Chem (version 4.2) data for Xiaoji (Conibear et al., 2018) to ensure consistency in model calibration and potential applications across China. The dataset provides grain yield components, including the number of ears per square metre, the number of grains per ear, and the grain dry matter (grain DM, in $\mathrm{g\,m^{-2}}$) (Feng et al., 2011, 2016). Additional physiological datasets (i.e. A_{net}, V_{cmax}, J_{max}, and $g_{\mathrm{H_2O}}$ (converted to $g_{\mathrm{O_3}}$ as described in Sect. S1b)) are also provided, but only for the year 2008 for all cultivars (Y2, Y19, Y15, and Y16) and for the flag leaf. The 2008 data also include measurements of chlorophyll (in $\mathrm{mg\,m^{-2}}$) which can be used to assess the level of senescence experienced by the leaf (Mariën et al., 2019). Since the year 2008 also showed significant differences in grain DM between AA and E O_3 treatments (a mean relative yield difference of 6.73 for all cultivars; see Table S2b), this year was used to train the DO_3SE-Crop model with other years (i.e. 2007 and 2009) used to test the model.

Further experimental details are provided in Feng et al. (2011, 2016). Table 1 describes the average, minimum,

and maximum values for all measured variables required to run the DO_3SE-Crop model collected at the Xiaoji site for each year. Additionally, the M7 (mean 7 h O_3 concentration over the exposure period in ppb) is included for both AA and E O_3 treatments. Measurements were taken at a height of 2 m above the ground surface.

3.2 DO_3SE-Crop calibration and evaluation

Development and calibration of the DO_3SE-Crop model with the Xiaoji experimental dataset followed three main steps: (i) sensitivity analysis to identify key model parameters to calibrate, (ii) calibration of these key parameters for a single year and both tolerant and sensitive cultivars, and (iii) evaluation of key DO_3SE-Crop model outputs for different years and cultivars from those used in model calibration.

To perform the sensitivity analysis we used the SALib Python library (Iwanga et al., 2022; Herman and Usher, 2017). The analysis requires ranges to be specified for the parameters (identified by an initial manual calibration) that are included in the sensitivity analysis. For physiological parameters, ranges were determined by considering the range of these parameters in the literature. For carbon allocation parameters, the range was identified by considering the maximum and minimum values of these parameters that would result in appropriate dry matter partitioning within the plant. Once the ranges were identified, the sensitivity analysis was run using the extended Fourier amplitude sensitivity analysis, which has been commonly used by other crop modellers to improve their calibrations (Silvestro et al., 2017; Vazquez-Cruz et al., 2014). From the sensitivity analysis outputs (see Fig. S6), the parameters whose variation contributes the most to variations in selected modelling outputs (in this case photosynthetic rate and yield) were identified as the key model outputs for calibration. Using this method we identified the following DO_3SE-Crop parameters as those most important to calibrate: (i) leaf photosynthesis parameters (V_{cmax25}, J_{max25}, kN, m, and VPD_0) and (ii) C allocation parameters (α_{root}, α_{leaf}, α_{stem}, Υ , τ) and related dark respiration coefficients (R_{dcoeff} and R_{gcoeff}) which were later included in the calibration after identifying issues with overestimated respiration, likely due to the use of parameter values designed for broad plant functional types, which may not be suitable for wheat. O_3 damage module parameters related to senescence (γ_3, γ_4, γ_5, and CLsO3) were not included in the sensitivity analysis, as γ_3 and CLsO3 are already recognised as important for calibration, and γ_4 and γ_5 were introduced in this study to represent the start (SOS) and end (EOS) of senescence, making both essential for calibration. Phenology parameters were also excluded as earlier studies have shown these are relatively straightforward to calibrate using automated methods for a range of environmental conditions (Nguyen et al., 2024). We note that assessing the probability distribution of these ranges would also be useful but consider this outside the scope of the current paper due largely to data limitations.

The DO_3SE-Crop model was then calibrated using the 2008 dataset for the Y2 and Y16 cultivars. The year 2008 was selected since this showed a substantial difference in yield of 208 and 148 g m^{-2} between the AA and EO_3 treatments for the Y2 and Y16 cultivars, respectively. These cultivars were chosen since they were identified as the most sensitive (Y2) and tolerant (Y16) cultivars according to the experimental analysis conducted by Feng et al. (2016). See Fig. 5, which shows a diagram representing the calibration process. Calibration of the phenology module used only the Y2 cultivar, AA O_3 treatment data describing the timing of emergence, anthesis, and maturity to calibrate key phenology parameters (T_b, T_0, T_m, VT_{min}, VT_{max}, PIV and PID, TT_{emr}, TT_{veg}, TT_{rep}, and T_l). The phenology calibration was automated by computationally applying a genetic algorithm (Wang, 1997), an optimisation technique with gradient decent to find the best parameters. This uses a combination of crossover strategy (selecting parameters randomly from parameter pairings) and mutation strategy (which takes a parameter range and uses incremental step changes) to identify the parameters which give the highest R^2 and lowest root mean square error (RMSE) when compared with observations of the timing (day of year) of anthesis and maturity.

Calibration of the leaf physiology, canopy C allocation, and O_3 damage DO_3SE-Crop modules was performed manually. This required that an initial value and range be defined for each parameter, which were defined from a combination of observations from the Xiaoji experimental dataset as well as values taken from the literature (see Tables A1 and A2 of the Appendix A for details). The model was manually calibrated until certain conditions were satisfied, as explained below. Calibration of the leaf physiology parameters (V_{cmax}, J_{max}, kN, m, and VPD_0) was performed only for the Y2 cultivar, AA O_3 treatment whilst keeping all other parameters fixed. This calibration aimed to achieve a maximum A_{net} value of 30 µmol CO_2 m^{-2} s^{-1} and a g_{O_3} value of 350 mmol O_3 m^{-2} PLA s^{-1}, consistent with the maximum values observed in the Xiaoji dataset (Zhu et al., 2011). We calibrated V_{cmax} and J_{max} as measurements are only provided for Y2 and Y16 cultivars and only for certain points during the growth period, and we know that V_{cmax} and J_{max} can vary seasonally.

Calibration of the C allocation parameters (α_{root}, α_{leaf}, α_{stem}, Υ, τ) and related dark respiration coefficients (R_{dcoeff} and R_{gcoeff}) was also performed keeping all other parameters fixed. This calibration aimed to achieve the following criteria: a stem dry matter to leaf dry matter ratio (R_{SL}) of approximately 2 : 1 (Huang et al., 2022), relative growth of different plant parts (i.e. leaves, stem, roots, grain) consistent with profiles found in the literature (Osborne et al., 2015; Penning de Vries, 1989), a modelled grain DM within ±30 % of the observed, an above-ground DM value of between 1200–1600 g m^{-2}, an LAI value between 4–7 m^2 m^{-2}, and an R_d

Table 1. Summary of hourly meteorological and ozone concentration ($[O_3]$) data at Xiaoji.

Variable	Unit	Description	Year 2007 (min, avg, max)	Year 2008 (min, avg, max)	Year 2009 (min, avg, max)
PAR_{total}	$W\,m^{-2}$	Direct and diffuse PAR at the top of the canopy	0, 241.94, 1759	0, 265.15, 1810.48	0, 262.16, 1850.5
T_{air}	°C	Surface air temperature in °C	−6.35, 10.07, 34.10	−9.22, 8.24, 32.7	−9.17, 9.62, 33.64
VPD	kPa	Leaf to air vapour pressure deficit	0, 0.34, 3.77	0, 0.3, 3.5	0, 0.38, 3.8
u_z	$m\,s^{-1}$	Wind speed at a reference height z	0.03, 2.14, 8.19	0.07, 2.11, 8.83	0.05, 2.10 8.45
C_z (and M7 value) for AA O_3 treatment	ppb	Ozone concentration at a reference height z	0, 15.48, 129.95 (47.2)	0, 16.2, 137.07 (49)	0, 15.9, 102.02 (47)
C_z (and M7 value) for E O_3 treatment	ppb	Ozone concentration at a reference height z	0, 16.83, 176.73 (56.1)	0, 17.46, 171.19 (60.7)	0, 17.95, 153.40 (58.7)
O_3 exposure period	Days		38	92	92

value of between 30 % and 60 % of A_{net} (Amthor et al., 2019). We calibrated C allocation parameters as the JULES-crop model calibration has only been performed for broad, global-scale application for wheat (Osborne et al., 2015) and therefore requires further calibration for application under Chinese conditions. Further, the observed dataset does not provide any information with regards to the change in carbon allocation parameters due to ozone. The C allocation parameters were only calibrated for ambient ozone conditions, and we only investigate the effect of ozone on C assimilation (not C allocation).

Finally, calibration of the O_3 parameters (γ_3, γ_4, and γ_5) was performed using 2008 data for the Y2 and Y16 cultivars whilst again keeping the other parameters fixed. Calibration was targeted so that the difference in grain DM between ambient and elevated O_3 treatments was as close as possible to ± 10 % of the observed.

The manual calibration process consisted of three stages as explained above, as well as comparisons with established information on wheat growth from the literature. By reducing the number of parameters involved in the calibration, the chance of equifinality (multiple combinations of parameters yielding similar results) was minimised (Beven, 2006). The parameters identified by the sensitivity analysis were varied within realistic ranges to obtain a parameterisation that closely approximates wheat physiological processes. Multiple parameterisations were tested to avoid convergence on local minima in R^2 and RMSE. While further fine-tuning of the parameter ranges could potentially improve yield prediction, it might also disrupt simulations of other key plant processes, such as carbon allocation or photosynthesis. The calibration approach balances the need for accurate output simulation with the physiological realism required for wheat growth under the conditions of this study. Though it is difficult to claim that the absolute optimal parameter set has been achieved, this limitation is common to any model calibration (Wallach, 2011). The current parameterisation represents a physiologically realistic simulation of wheat growth under the conditions of the present study using a robust calibration method.

Evaluation of the DO_3SE-Crop model was conducted using Xiaoji data for 2007 and 2009 for all cultivars and 2008 data for Y19 and Y16 cultivars. This evaluation tested the ability of the calibrated DO_3SE-Crop model to simulate grain DM using R^2 and RMSE statistical tests.

4 Results

We first examine the model's ability to simulate the key phenological development stages since this is key to simulating the variation in C allocation to different plant parts over the course of the growing season and hence how O_3 exposure will influence growth and yield which is determined by the timing and length of the grain-filling period. We also explore how DO_3SE-Crop simulates within-canopy $[O_3]$ profiles to understand which layers of the canopy are most important in determining O_3 response. We then examine the ability of the model to simulate leaf-level physiology and C allocation to the different parts of the crop. Lastly, the impact of both instantaneous and long-term O_3 damage on the crop's final grain DM is evaluated for different cultivars and years.

i. Crop phenology

The Xiaoji dataset provides sowing and harvest dates for all cultivars for each year but only provides the date of the tim-

ing of anthesis for the years 2008 and 2009 for all cultivars. We assume that DVI = 1 is equivalent to the start of anthesis and that this occurs 4–5 d after flag leaf emergence as shown in Fig. 2. We determine the influence of O_3 on the start and end of senescence (SOS and EOS) using the breakpoint method (described in Pande et al., 2024) to assess significant changes in the chlorophyll values that indicate senescence onset and rate of change for the quantification of tl_{ep} and tl_{se}. This method is applied to chlorophyll data collected in 2008 under both AA and E O_3 treatments for the Y2 cultivar. We then assume that these key phenology parameters (i.e. TT_{emr}, TT_{veg}, TT_{rep}, tl_{ep}, and tl_{se}) are consistent across cultivars and years. Our results in Fig. 3 suggests this is a reasonable assumption; however, we appreciate that assuming these phenology parameters will work for a wider variety of cultivar types (e.g. early or late sown and/or maturing) and years with rather different meteorological conditions needs to be done with caution.

Figure S1 shows the modelled vs. observed timing of anthesis and harvest for the training dataset. Figure 3 shows the same for the test dataset. For the test dataset there is a variation of 2 to 4 and 1 to 6 d for the modelled anthesis and maturity in relation to observed anthesis and maturity, respectively, with observed phenology tending to be a little later than modelled. The T_l ranges between 1325 and 1478 °C days for the 3 years, with crop sowing occurring between 315 and 324 d of year and harvests occurring between 135 and 151 d of year (of the following year). The number of days from the modelled crop sowing to harvest was between 181 and 191 for the 3 years, compared to 198 and 201 for the observations.

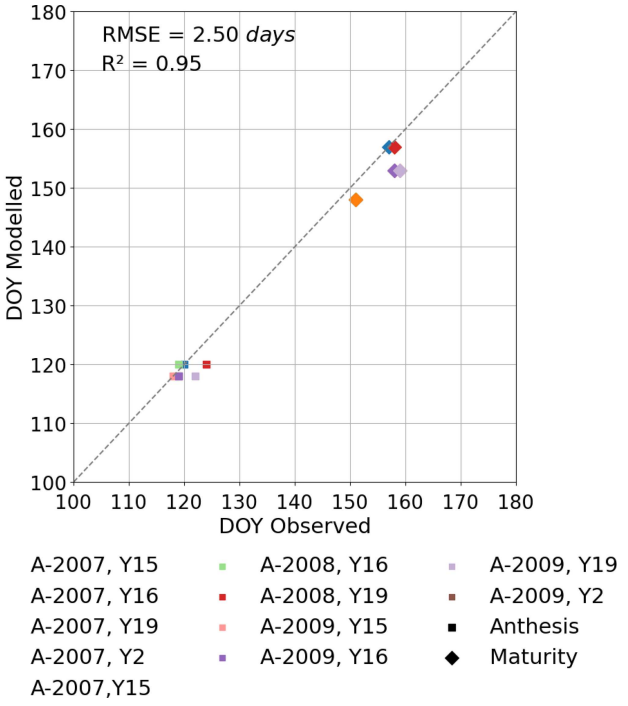

Figure 3. Modelled vs. observed phenological stages provided as day of year (DOY) for the test dataset (i.e. excluding the year 2008 for the Y2 cultivar).

ii. Leaf physiology variables (A_{net}, g_{O_3})

The DO_3SE-Crop model was able to simulate the seasonal A_{net} and g_{O_3} with values ranging from 0 to 27 µmol CO_2 m^{-2} s^{-1} and 10 to 351 mmol O_3 m^{-2} s^{-1} for A_{net} and g_{O_3}, respectively, over the course of the growing season (see Fig. 4). The simulated daily maximum values of modelled g_{O_3}, at 351 mmol O_3 m^{-2} s^{-1}, were within the range of the observed value of 340 mmol O_3 m^{-2} s^{-1}. Similarly, the modelled daily maximum A_{net} is 27 µmol CO_2 m^{-2} s^{-1} compared to observed value of 28 µmol CO_2 m^{-2} s^{-1} for the period between anthesis and 10 d before maturity for the year 2008, for the Y16 cultivar (similar results were obtained for the Y2 cultivar; see Fig. S5). In Fig. 4a and b, the steep decline in modelled A_{net} and g_{O_3} is not seen in the observed dataset. This discrepancy may occur since the simulated A_{net} and g_{O_3} values represent sunlit parts of the upper canopy which comprise both green and senesced leaf material. In contrast, observed A_{net} and g_{O_3} values are measured specifically on the flag leaf and most likely only for the green parts of the leaf, since the LI-6400 photosynthesis system mounted with a 6400–40 leaf chamber fluorometer (used to measure A_{net} and g_{O_3} in the Xiaoji experiment, Feng et al., 2016) will not provide values for senesced leaf material. See also Fig. 4, which combines A_{net} and g_{O_3} with observed normalised chlorophyll content and clearly shows the leaf is senescing as predicted by the model. However, the observed decline in chlorophyll values closely matches the decrease in modelled A_{net} and g_{O_3}, with the model accurately capturing the timing of the earlier onset of senescence, which occurred 0–3 d earlier in the AA and EO_3 treatments. It is useful to note that the calibrated V_{cmax} and J_{max} values match the observed values within ±2 µmol CO_2 m^2 s^{-1}.

iii. Within-canopy variation in O_3 and physiology

An important determinant of O_3 deposition and damage is stomatal O_3 deposition (our gO_{3c}), which is a function of within-canopy transfer of O_3 and stomatal and non-stomatal deposition. The multi-layer aspect of the DO_3SE-Crop model allows within-canopy stomatal and non-stomatal O_3 deposition to be simulated. Figure 5 shows the variation in key variables that determine total and stomatal O_3 canopy deposition across four canopy layers as a midday average over the course of the tl_{ep} period of the flag leaf, for the year 2008 and the Y16 cultivar.

Figure 5a shows a decrease of within-canopy O_3 concentration from highs of around 140 ppb to values within the range of 10 to 50 ppb between the top of the canopy and bottom canopy layer; the penetration of O_3 into the canopy

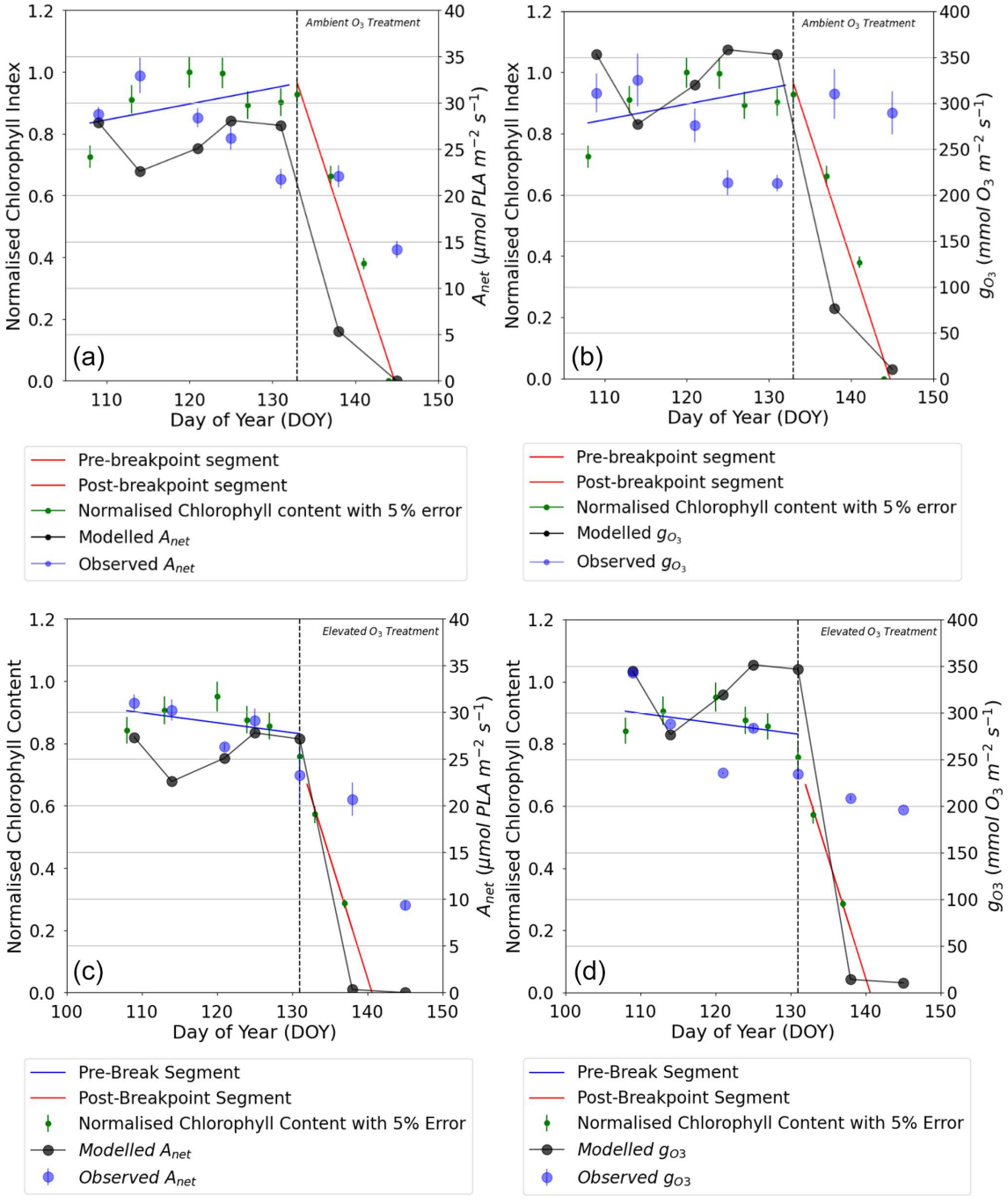

Figure 4. Comparison of daily maxima seasonal profiles of DO$_3$SE-Crop modelled canopy leaf vs. observed flag leaf data for **(a)** AA O_3 treatment A_{net}, **(b)** AA O_3 treatment g_{O_3}, **(c)** E O_3 treatment A_{net}, and **(d)** E O_3 treatment g_{O_3} for the period from the anthesis (i.e. TT_{rep}) for the year 2008 and the Y16 cultivar. The left (solid blue line) and right (solid red line) represent the segment fits to the normalised chlorophyll content values for application of the breakpoint method to define the SOS (start of senescence) shown as the dashed black line. The green scatter solid dots, along with their standard measurement error, represent the normalised observed chlorophyll content values (see Fig. 7 for further details).

increases over time as the canopy senescence and O_3 uptake is reduced. Similarly, PAR_{sun} is reduced from maximum values of around 200 W m^{-2} at the top of the canopy to values of around 100 W m^{-2} in the lower canopy layers even on sunny days (see Fig. 5c). The leaf rb_{O_3} (Fig. 5b) increases with canopy depth with resistances in the region of approximately 50 s m^{-1} at the top of the canopy to values of around 600 s m^{-1} at the bottom of the canopy; this will limit stom-

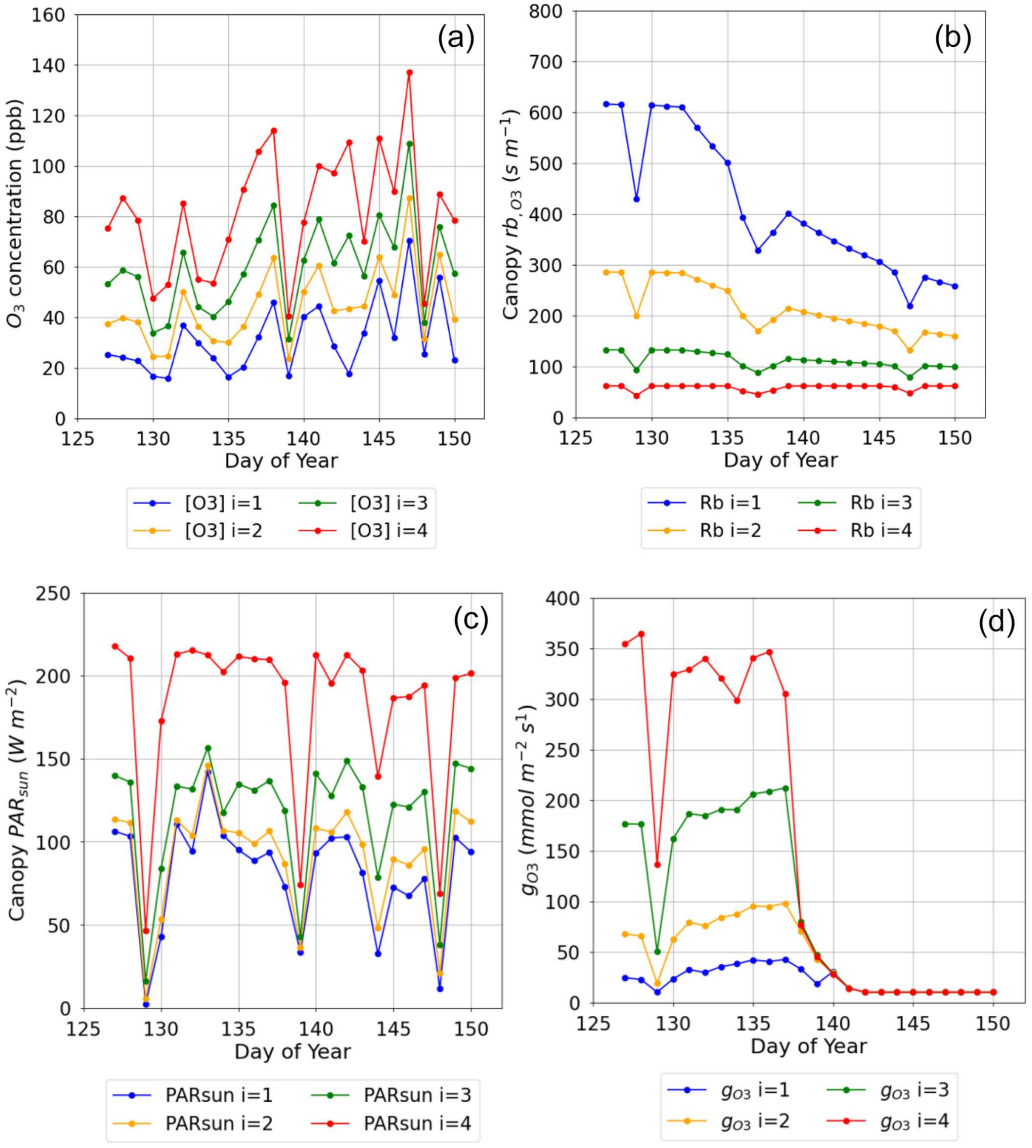

Figure 5. Plot showing variation in key O_3 deposition terms as daily maxima by canopy layer (NB $i = 4$ is the top canopy layer, $n = 4$) **(a)** O_3 concentration at the top of each layer, **(b)** leaf boundary layer resistance by canopy layer ($rb_{,O_3}$), **(c)** PAR for the sunlit LAI component of each layer (PAR_{sun}), and **(d)** leaf-level stomatal conductance to O_3 (g_{O_3}) for the period from anthesis (i.e. TT_{rep}) for the Y16 cultivar and for the E O_3 treatment in 2008.

atal O_3 uptake in the lower canopy layers; finally, these factors combine to influence canopy level g_{O_3} (Fig. 5d), which is reduced from values of around 350 at the top of the canopy to 20 nmol O_3 m^{-2} s^{-1} at the bottom of the canopy layer; these differences in leaf rb_{O_3} and g_{O_3} are reduced with the onset of senescence. This analysis shows the importance of interplay between these different factors for an accurate whole-canopy estimate of O_3 deposition.

iv. Crop development, biomass, and yield

The dry matter dynamics of the different parts of the crop are shown in Fig. 6. The modelled grain DM value of 851 g m^{-2} was reasonably close to the observed value of 888 g m^{-2}. The stem to leaf dry matter ratio (R_{SL}) is 2.1 : 1 and therefore in the range provided in the literature (Huang et al., 2022). The above-ground biomass values of 1510 g m^{-2} also match reasonably well against the 1200 to 1600 g m^{-2} range described in the literature (Huang et al., 2022; Liu et al., 2022). Further, the partition fraction profiles are consistent with those of Osborne et al. (2015) as shown in Fig. 6a, with the main differences being that the modelled stem and root partition profiles are somewhat higher and lower, respectively. The JULES model comparison is provided for illustrative purposes only (i.e. this model has not been calibrated with the Xiaoji data

Table 2. Simulations of percent of grain DM loss that compare ambient (AA) and elevated (E O_3) treatments with a pre-industrial O_3 scenario divided between grain DM losses caused by the instantaneous effect O_3 on photosynthesis and the long-term O_3 effect on senescence. The effects of both damage O_3 mechanisms acting together are also shown.

Year	Tolerant: instantaneous O_3 effect on % grain DM		Tolerant: long-term O_3 effect on % grain DM	
	Ambient versus pre-industrial	Elevated versus pre-industrial	Ambient versus pre-industrial	Elevated versus pre-industrial
2007	0	0.01	16.60	29.05
2008	0	0	9.85	24.37
2009	0.01	0.01	17.48	25.87
	Sensitive: instantaneous O_3 effect on % grain DM		Sensitive: long-term O_3 effect on % grain DM	
	Ambient versus pre-industrial	Elevated versus pre-industrial	Ambient versus pre-industrial	Elevated versus pre-industrial
2007	0	0.2	18.43	31.13
2008	0	0	13.43	29.14
2009	0.03	0.03	19.5	28.11

but rather is a parameterisation suggested for global application).

v. O_3-induced yield loss difference between tolerant and sensitive cultivars: instantaneous and long-term senescence impact

The grain DM is assumed to be damaged by both the instantaneous impact of O_3 (Farage et al., 1991) on photosynthesis and a longer-term O_3 effect that can lead to enhanced senescence (Y. Feng et al., 2022). To explore which of these damage mechanisms is most important, we calculated the difference in the grain DM caused by carbon assimilation for the AA and E O_3 treatments as compared to a simulated very low O_3 treatment representing pre-industrial conditions (for which C_z O_3 concentration did not exceed 15 ppb) for the tolerant (Y16) and sensitive (Y2) cultivar for each of the 3 years (see Table 2). We found a negligible effect of O_3 (0 % to 0.2 %) on grain DM due to the instantaneous effect of O_3 on photosynthesis, which could perhaps be partly due to the to the crops ability to recover photosynthetic capacity overnight, compared to a highly significant (9.85 % to 31.13 %) impact due to the long-term O_3 effect on carbon assimilation via the enhancement of senescence on final grain DM. Table S3 shows the observed percent of grain DM loss compared to a modelled pre-industrial O_3 scenario due to the combination of instantaneous and long-term ozone effect.

vi. Senescence

The breakpoint method (Mariën et al., 2019) was used to determine the onset (SOS) and end (EOS) of senescence and maturity, respectively, using the chlorophyll data which were available for the year 2008 and the Y16 and Y2 cultivars. Results in Figs. 7 and S4 show that the E O_3 treatment for cultivars Y16 and Y2 brought forward the SOS by 3 and 5 d (see Fig. 7), respectively, and EOS by 6 and 9 d (see Fig. S4), respectively. Figure 7 also shows the f_{LS} profile which denotes the DO_3SE-Crop models' accumulated stomatal O_3 flux effect on senescence; it is clear that f_{LS} is able to simulate the change in normalised chlorophyll content reasonably well. The slope of the ambient f_{LS} is already steep since the ambient treatment already has rather high O_3 levels as is now made clear in Table 1 with a value of 47 ppb. According to the M7 wheat dose–response relationship this would result in a yield loss of $\sim 5\,\%$.

vii. Grain DM simulations across years and between cultivars

Figure 8 shows a box plot of the modelled vs. observed grain DM for the sensitive (Y2, Y19) and tolerant (Y15, Y16) cultivars for each O_3 treatment (AA and E) for the years 2007, 2008, and 2009 (i.e. all data). Given the variability in the experimental data, the model simulates the difference in grain DM between the AA and E O_3 treatments reasonably well with a simulated reduction in grain DM of 29 to 131 $g\,m^{-2}$ compared with observed values of 81 to 165 $g\,m^{-2}$ for the tolerant cultivars and 49 to 196 $g\,m^{-2}$ compared with observed values of 54 to 293 $g\,m^{-2}$ for the sensitive cultivars, respectively. The most notable difference is that there is a larger range in the simulated grain DM losses of the modelled sensitive cultivars, though the simulated mean value for absolute grain DM suggests a more conservative influence of O_3, with yields at 610 $g\,m^{-2}$ vs. observed average yields of 590 $g\,m^{-2}$.

Finally, Fig. 9 shows the relationship between modelled vs. observed grain DM (in $g\,m^{-2}$) as a scatter plot; a linear regression through these data gives an R^2 value of 0.68 and RMSE of 76 $g\,m^{-2}$, showing the model is able to simulate with reasonable accuracy the differences in absolute

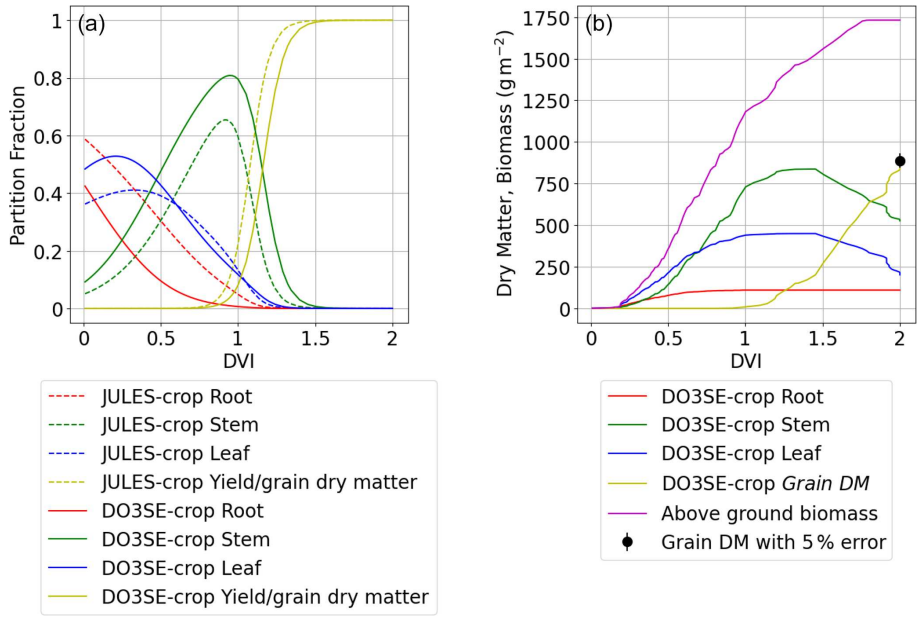

Figure 6. Seasonal profiles (i.e. plotted against DVI) of carbon allocation variables for the Xiaoji calibrated DO$_3$SE-Crop model (i.e. AA O$_3$ treatment, year 2008, and Y16 cultivar) with panel **(a)** showing the partition fractions of the daily accumulated NPP partitioned to roots, stems, leaves, and grains for the Xiaoji calibrated DO$_3$SE-Crop model (solid lines) vs. the JULES-crop model (dashed line) calibrated for global application after Osborne et al. (2015) and panel **(b)** showing the DM (in g m^{-2}) of daily accumulated NPP partitioned to roots, stems, leaves, and grains, with the observed final grain DM for Y16 cultivar in 2008 also shown (solid black dot with 5 % error).

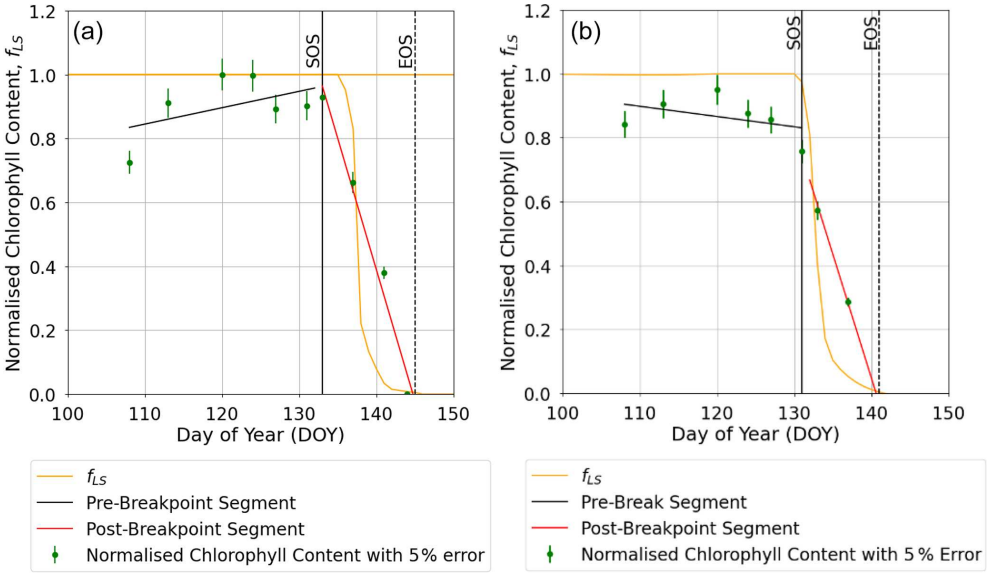

Figure 7. Profiles of O$_3$-induced leaf senescence for the Y16 cultivar for the **(a)** AA O$_3$ treatment and **(b)** E O$_3$ treatment. The timing of the SOS (solid black line) and EOS (dashed black line) was determined by applying the breakpoint method to the chlorophyll data and is shown in relation to the f_{LS} simulations of senescence (solid yellow line). The observed normalised chlorophyll content data, shown as filled green symbols, include error bars representing the standard deviation of the measurements.

yield for different cultivars and for different years. There are some instances of both underestimation and overestimation; however, the deviations from the 1 : 1 line are not excessively large. These models test results compare with an R^2 of 0.92 ($n = 4$) and an RMSE of 25.49 g m^2 for the training dataset (Y2 and Y16 cultivar and year 2008; see Fig. S3); the stronger agreement between observed and modelled training dataset, as well as the reasonable agreement for the entire

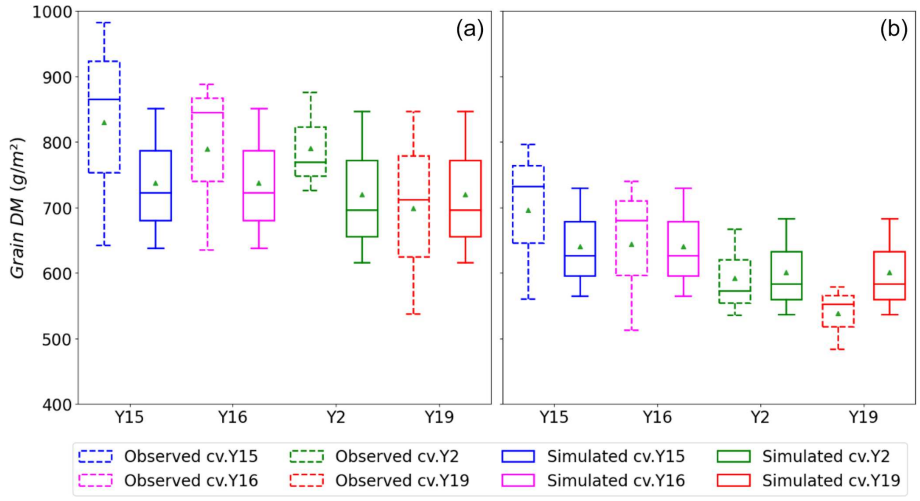

Figure 8. Box plots (crosses: 0.01 and 0.99 percentiles; box: 0.25 quartile, median, and 0.75 quartile; triangle: mean) of simulated and observed wheat grain DM for the tolerant (Y15 and Y16) and sensitive (Y2 and Y19) cultivars under **(a)** AA and **(b)** E O_3 treatment for the years 2007, 2008, and 2009; these data include the whole dataset.

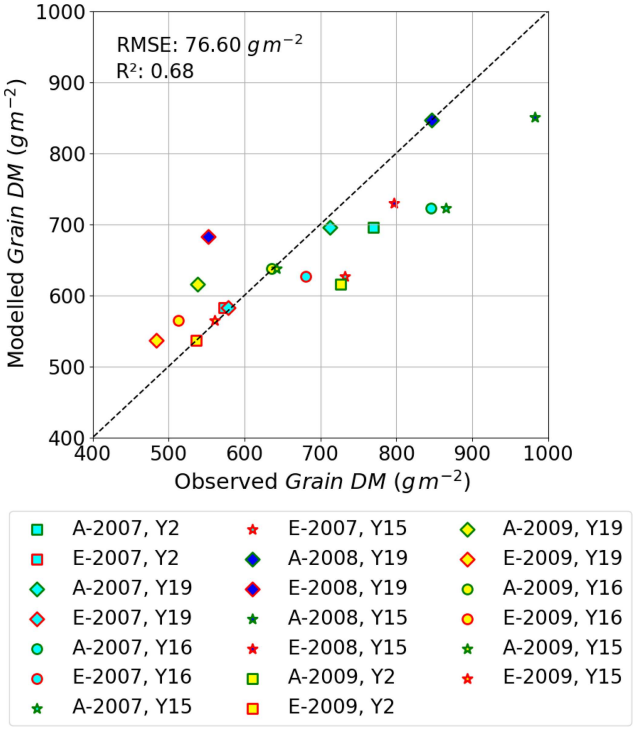

Figure 9. A scatter plot showing modelled vs. observed grain DM (in g m^{-2}) for the AA and E O_3 treatments for all four cultivars and 3 years of the Xiaoji dataset; these data include those used for evaluation.

dataset, would suggest the model is not over-fitted. We find that we tend to underestimate the O_3-induced relative yield loss (RYL) by between −2.76 and 15.34 % (observed minus modelled RYL) across all years and cultivars.

5 Discussion

The DO$_3$SE-Crop model was found capable of simulating O_3 damage to grain yield for O_3-FACE conditions at the experimental site in Xiaoji, China, with a good degree of accuracy. Simulated relative yield losses (RYLs) between AA and E O_3 treatments for all years ranged from 11 % to 14 % and from 13 % to 19 % for tolerant and sensitive cultivars, respectively; these tend to be lower (particularly for the more extreme O_3-induced yield losses of the sensitive cultivars) than the observed values of 13 % to 20 % and 10 % to 35 %. Overall, simulations of tolerant and sensitive cultivars underestimated RYLs by 4 % and 7 %, respectively, on average across years and cultivars (see data in Sect. S6). This would suggest that O_3-induced yield losses can be more reliably modelled for tolerant cultivars, possibly because additional processes causing O_3-induced yield losses in sensitive cultivars are not captured. Such processes might include the effect of O_3 on the allocation of carbon to different plant parts (Feng et al., 2008) or O_3 inducing additional respiratory costs via the up-regulation of defence mechanisms (Biswas et al., 2008). The model was also able to simulate absolute grain DM reasonably well. Under AA O_3 levels, grain DM simulated for all years and cultivars was between 616 and 851 g m^{-2} compared to observations of between 537 and 982 g m^{-2}. There is a tendency to overestimate grain DM under ambient conditions and underestimate grain DM under elevated O_3, which is reflected in the RYL values.

Overall, the DO$_3$SE-Crop model simulation results compare favourably to results made by the MCWLA-Wheat model (Tao et al., 2017), which was also calibrated for the Xiaoji experimental conditions but without distinction between tolerant and sensitive varieties. MCWLA-Wheat simulations of absolute yield varied from ∼ 5700 to 9000 kg ha^{-1}

(compared to ~ 5700 to $9800\,kg\,ha^{-1}$) for ambient and from ~ 4800 to $8000\,kg\,ha^{-1}$ (compared to ~ 5200 to $8000\,kg\,ha^{-1}$) for elevated O_3 treatments. A mean relative yield loss of 14 % was simulated by the model.

It is useful to set these site-specific estimates of O_3-induced yield losses in the context of yield losses estimated using more traditional, concentration-based O_3 risk assessment methods. A seminal paper by Z. Feng et al. (2022) estimated mean relative yield losses across East Asia due to ambient O_3 concentrations at 33 % (with a mean range of 28 % to 37 %) according to a mean monitored O_3 concentrations of 30.9 ppm h expressed as AOT40 (6-month accumulated daytime O_3 concentration above a threshold of 40 ppb). The mean difference in AOT40 (accumulated over only 75 d) between the AA and E O_3 treatments at Xiaoji across all years was 7.8 ppm h, giving a mean relative yield loss of approximately 10 % to 20 % depending on year and cultivar. As such, our modelled results in terms of RYLs between AA and E O_3 treatments are consistent with these broader results for East Asia.

Crop phenology plays a crucial role in determining the timing of the important O_3 exposure period (i.e. from anthesis to maturity) and hence O_3 damage. Evaluation of the DO_3SE-Crop phenology model shows the model is able to accurately simulate crop phenology for the 3 years at Xiaoji ($R^2 = 0.95$ and RMSE = 2.5; see Fig. 3). Estimating the correct timing of anthesis is crucial since the period from anthesis to crop maturity is the O_3-sensitive period. During this period, accumulated stomatal O_3 flux (acc_{fst}) will contribute to early and enhanced senescence once the critical threshold (CLsO3) is exceeded. This period also coincides with carbon accumulation in the grain (Kohut et al., 1987; Feng et al., 2008), which may be limited by O_3-induced early onset or enhanced senescence. The DO_3SE-Crop model was developed to accommodate the full range of effects of O_3 on senescence with revised functions, similar to those first developed by Ewert and Porter (2000), and was able to modify both the O_3-induced onset of senescence and the O_3 effect on maturity. This is important since experimental evidence has shown that O_3 can bring forward the maturity date; for example, the flag leaf was found to have senesced 25 d earlier in a high-O_3 treatment, compared to a charcoal-filtered treatment (Grandjean and Fuhrer, 1989; Gelang et al., 2000). O_3 was also found to cause differences in the time to maturity of the flag leaf, with Shi et al. (2009) reporting that maturity was brought forward by 8 d under an elevated O_3 treatment (50 % higher than ambient). Currently, other crop models with O_3 damage functions (e.g. MCWLA-Wheat (Tao et al., 2017) and LINTULCC-2 (Y. Feng et al., 2022)) are only able to bring the O_3-induced onset of senescence earlier.

The DO_3SE-Crop model is also able to simulate differential O_3 uptake in each canopy layer. Figure 5 shows that the majority of stomatal O_3 uptake occurs in the sunlit layers of the upper canopy. Similar results were found in an experimental study on a productive grassland in Switzerland; Jaggi et al. (2006) found that different levels of O_3 exposure to canopy components predominantly located in the upper and lower parts of the canopy support a multi-layer approach to modelling O_3 uptake. Therefore, the focus on the upper canopy by flux-based O_3 metrics (e.g. the phytotoxic ozone dose POD_y; LRTAP, 2017) seems rational in the absence of multi-layer modelling. Crop models such as LINTULCC-2 (Y. Feng et al., 2022) also focus on estimating stomatal O_3 uptake at the top of the canopy to estimate O_3-induced yield losses. For wheat, such an approach is further supported by the fact that the upper canopy layers consist of the flag leaf, which plays a crucial role in photosynthesis and grain filling (Pleijel et al., 2007). The multi-layer functionality of the DO_3SE-Crop model may, however, become more useful when considering crops that partition assimilated carbon to harvest organs earlier in their growing season such as potato (Okrah et al. 2023).

Our results show that the DO_3SE-Crop model was able to estimate the seasonal course of leaf A_{net} and g_{O_3} daily maxima observed at the Xiaoji site (see Fig. 4a) and when compared to other literature describing leaf physiological variables (Guan et al., 2015; Li et al., 2022). This suggests the coupled A_{net}–g_{sto} model is working for Chinese conditions (having previously been applied to and evaluated for European O_3 experimental conditions – see Pande et al., 2024). The leaf physiology parameters used in this study (i.e. for Asian conditions and cultivars) are higher than parameters for European studies. For Europe, V_{cmax} values of between 60 and $90\,\mu mol\,CO_2\,m^{-2}\,s^{-1}$ were found in the literature (Y. Feng et al., 2022; Pande et al., 2024; Van Oijen and Ewert, 1999) compared to the observed mean maximum value of $137\,\mu mol\,CO_2\,m^{-2}\,s^{-1}$ at Xiaoji which was used in this study. Similarly, European J_{max} values ranged from 160 to $180\,\mu mol\,CO_2\,m^{-2}\,s^{-1}$ (Feng et al., 2021; Pande et al., 2024; Van Oijen and Ewert, 1999) compared to the observed Xiaoji mean maximum value of $228\,\mu mol\,CO_2\,m^{-2}\,s^{-1}$. Even though these leaf physiology parameters are higher, absolute yields for these Chinese cultivars are consistent with those found under European conditions. This most likely reflects the importance of other environmental conditions (e.g. high vapour pressure deficits) limiting leaf carbon assimilation. Moreover, the complex interactions between O_3 exposure and the plants' physiological responses also play a crucial role. Ozone significantly affected antioxidative enzymes, thereby limiting overall photosynthetic efficiency and yield, particularly in O_3-sensitive cultivars, despite their ability to maintain high carboxylation capacity.

Ensuring the seasonal variation in carbon allocation to the different components of the crop (i.e. roots, stem, leaves, and harvest organs) is essential for the simulation of crop growth and yield. There are limited data in the literature that provide these variables, so we compare our results to the carbon allocation profiles described for wheat provided in the original JULES-crop model description, recognising this is intended for wheat grown globally. The DO_3SE-Crop model carbon

allocation to the stem and roots is comparatively higher than what was simulated by JULES-crop (Osborne et al., 2015; see Fig. 6a). However, we can justify the carbon allocation coefficients used for Xiaoji since the DO_3SE-Crop model was able to distribute carbon to different plant components to produce a well-proportioned plant over the course of the growing season; this was determined by the calibration to a number of key crop variables (i.e. ratios of plant respiration, LAI, stem to leaf dry matter, above-ground components, and grain dry matter). Importantly, when applied to the test dataset (i.e. excluding 2008 data for the Y2 and Y16 cultivar), the model was found to simulate the grain dry matter under ambient and elevated O_3 treatments to within 7.9 %–8.7 % of the observed values ($R^2 = 0.68$, 76 g m^{-2} see Fig. 9).

The DO_3SE-Crop model, similar to other crop models with O_3 damage functions (i.e. MCWLA-Wheat (Tao et al., 2017), LINTULCC-2 (Y. Feng et al., 2022), and WOFOST (Nguyen et al., 2024)) has the capacity to simulate both the instantaneous and long-term O_3 impact on wheat grain yield. The instantaneous O_3 effect on photosynthesis may cause leaf cell damage and decrease the supply of carbohydrate precursors, which can significantly decrease g_{O_3}, V_{cmax}, and leaf chlorophyll content (Farage et al., 1991). Elevated O_3 also leads to generation of reactive oxygen species (ROS) in plant cells, which can cause oxidative damage to various cellular components. Rubisco, the enzyme responsible for carbon fixation in the photosynthetic process, can be particularly susceptible to this damage, leading to a reduced carboxylation rate (V_{cmax}). Such an O_3 effect on V_{cmax} reduces net photosynthesis and can also induce early senescence, shortening the grain-filling period (Triboi and Triboi-Blondel, 2002).

Results from the DO_3SE-Crop model found a larger impact on yield due to the long-term O_3 impact causing relative yield loss of between 10 % and 31 % compared to only between 0 % and 0.2 % resulting from the instantaneous O_3 impact on photosynthesis. Previous studies have also found that the long-term O_3 effect has a larger impact on yield compared to the instantaneous effect of O_3 on photosynthesis (Emberson et al., 2018; Brewster et al., 2024). Senescence is an age-dependent process of degradation and degeneration that allows nutrients to be re-distributed to different plant organs (Lim et al., 2007). Under O_3 stress, this process is often found to occur earlier and more rapidly in leaves as well as at the whole-plant or crop canopy scale (Brewster et al., 2024). The causes of this early and accelerated senescence are not completely understood but may be related to O_3-induced enhanced expression of many genes involved in natural senescence (Miller et al., 1999). Elevated O_3 was also found to inhibit sugar export from leaves (Yadav et al., 2020; Feng et al., 2024), which could trigger early onset of leaf senescence.

The DO_3SE-Crop model accounts for the impact of O_3 on the rubisco enzyme by incorporating modified (Ewert and Porter, 2000) functions for instantaneous and long-term O_3 impact on V_{cmax} as an important parameter used to characterise the crop photosynthetic capacity (Ewert and Porter, 2000; Osborne et al., 2019). The DO_3SE-Crop model assumes that the O_3 will only accumulate on exceedance of a stomatal O_3 flux threshold of 6 nmol O_3 m^{-2} s^{-1}. The long-term O_3 impact mechanism of the DO_3SE-Crop model simulated the effect of senescence on V_{cmax} reasonably well as evidenced by the reduction in leaf chlorophyll content. We used the breakpoint method (Yang et al., 2016; Mariën et al., 2019) to estimate the SOS and EOS using the day of the year and measured chlorophyll content (Figs. 7 and S4). It is crucial to accurately model the timing of SOS and EOS correctly as this determines the O_3 effect on the duration of the grain-filling period and hence the difference in yield loss due to different O_3 treatments. For example, we modelled a difference of 3 to 5 d in SOS and 6 to 9 d in EOS on average across years for the sensitive and tolerant cultivar, respectively.

China's wheat breeding programme has seen more than 1850 varieties used across China between the 1920s and 2014, leading to increased yields from less than 1 to more than 5 t ha^{-1} (Qin et al., 2015). Here, albeit with an extremely limited dataset, we parameterise the DO_3SE-Crop model for tolerant and sensitive wheat crop cultivars, since many experimental studies have shown that the response of different cultivars to O_3 stress differs (Biswas et al., 2008). Based on the available data, the model seemed able to capture the difference in grain dry matter between these different cultivar groups across different years reasonably well when compared to the observed dataset ($R^2 = 0.68$; see Fig. 8). Such a cultivar sensitivity-based parameterisation can provide additional information on the certainty of regional yield loss estimates given the large number of wheat varieties grown across China. However, when applying the model to a broader region, it would be advisable to calibrate phenology for different agro-ecological zones as the temperature changes across China, impacting the duration of the key phenological stages such as anthesis and maturity (Luo et al., 2021). Additionally, carbon allocation parameters may need adjustment, as studies have shown changes in dry matter content across different agro-ecological zones (Hussain and Bangash, 2017).

6 Conclusions

We have shown that the newly developed DO_3SE-Crop model can be calibrated for O_3-tolerant and sensitive wheat varieties for O_3-FACE site conditions at Xiaoji in China. The model can simulate crop phenology, leaf physiology, crop growth, and yield reasonably well across different years. The model is also able to simulate the effect of O_3 stress on grain yield distinguishing the extent of O_3 damage resulting from the same O_3 treatment on cultivars with differing O_3 sensitivities. The DO_3SE-Crop model also has the advantage of simulating O_3 transfer and deposition dynamics within the wheat crop canopy, which could in the future improve our understanding of whole-canopy O_3 effects for crops with dif-

ferent carbon allocation profiles. The ability of the model to estimate relative yield losses across years also suggests the model is fit for purpose to assess the effects of O_3 under a variety of climate variable and O_3 concentration conditions.

Appendix A

Table A1. DO_3SE-Crop variables.

Variable	Unit	Description
T_{eff}	°C days	Effective temperature accumulated between sowing to maturity
DVI	–	Development index
T_{air}	°C	Surface air temperature in degrees Celsius
$T_{\text{air,k}}$	°K	Surface air temperature in kelvin
T_{min}	°C	Daily minimum surface air temperature
T_{max}	°C	Daily maximum surface air temperature
LTT	°C d	Thermal time accumulated by a leaf
V_{dd}	days	Accumulated vernalised days
V	days	Vernalised days
V_d	days	Devernalised days
VF	–	Vernalisation factor
PP	h	Photoperiod
PF	–	Photoperiod factor
A_{net}	$\mu\text{mol CO}_2\ \text{m}^{-2}\ \text{s}^{-1}$	Net photosynthesis or rate of CO_2 assimilation
A_c	$\mu\text{mol CO}_2\ \text{m}^{-2}\ \text{s}^{-1}$	RuBP (ribulose-1,5-bisphosphate) limited A_{net}
A_j	$\mu\text{mol CO}_2\ \text{m}^{-2},\text{s}^{-1}$	Electron transport limited A_{net}
A_{p}	$\mu\text{mol CO}_2\ \text{m}^{-2}\ \text{s}^{-1}$	TPU (triose phosphate) limited A_{net}
R_{d}	$\mu\text{mol CO}_2\ \text{m}^{-2}\ \text{s}^{-1}$	Dark respiration
f_{PAW}	–	Fraction of plant available water
PAW_{t}	–	Threshold of PAW, above which g_{sto} is at a maximum as described in the f_{PAW} function
PAW	$\text{m}^3\ \text{m}^{-3}$	Plant available water
C_{i}	$\mu\text{mol mol}^{-1}$	Intercellular CO_2 partial pressure
O_{i}	mmol mol^{-1}	Intercellular O_2 concentrations
Γ^*	$\mu\text{mol mol}^{-1}$	CO_2 compensation point in the absence of respiration
Γ	$\mu\text{mol mol}^{-1}$	CO_2 compensation point
J	$\mu\text{mol CO}_2\ \text{m}^{-2}\ \text{s}^{-1}$	Electron transport rate
VPD	kPa	Leaf to air vapour pressure deficit
C_z	ppb	O_3 concentration at reference height z
C_{h}	nmol m^{-3}	O_3 concentration at the crop canopy height
C_{zh}	nmol m^{-3}	O_3 concentration at the top of the crop canopy height
C_{zb}	nmol m^{-3}	O_3 concentration at the bottom of the crop canopy height
f_{st}	$\text{nmol O}_3\ \text{m}^{-2}\ \text{s}^{-1}$	Leaf-level stomatal O_3 flux
accf_{st}	$\text{mmol O}_3\ \text{m}^{-2}$	Accumulated stomatal O_3 flux
C_{l}	$\text{nmol O}_3\ \text{m}^{-3}$	O_3 at the upper surface of the laminar layer of a leaf
$f_{\text{O}_3,\text{s}}(d)$	–	Effect of daily cumulative stomatal O_3 flux on Vc_{max}
$f_{\text{O}_3,\text{s}}(h)$	–	Effect of hourly cumulative stomatal O_3 flux on Vc_{max}
$f_{\text{O}_3,\text{s}}(d-1)$	–	Previous day's effect of cumulative stomatal O_3 flux on Vc_{max}
$r_{\text{O}_3,\text{s}}$	–	Incomplete overnight recovery of O_3 affected Vc_{max}
f_{LA}	–	Leaf-age-related capacity to recover from accumulated stomatal O_3 flux
$fO3_l$	–	Weighted accumulated stomatal O_3 flux that determines the onset of leaf senescence
f_{LS}	–	Accumulated stomatal O_3 flux effect on leaf senescence
tl	°C days	Effective temperature accumulated by a leaf after emergence (DVI = 0)
tl_{ep}	–	Effective temperature accumulated by a leaf between full expansion and the onset of leaf senescence
$tl_{\text{ep}_{\text{O}_3}}$	–	Effective temperature accumulated by a leaf between full expansion and the onset of leaf senescence brought forward by O_3

Table A1. Continued.

Variable	Unit	Description
tl_{se}	–	Effective temperature accumulated by a leaf between the onset of leaf senescence and maturity
$tl_{se_{O_3}}$	–	Effective temperature accumulated by a leaf between the onset of leaf senescence and maturity brought forward by O_3
g_{CO_2}	µmol CO_2 m^{-2} PLA s^{-1}	Stomatal conductance to CO_2
f_{VPD}	–	Relationship between VPD and relative stomatal conductance
c_s	mol CO_2 mol^{-1}	External CO_2 concentration at the leaf surface
c_a	mmol CO_2 mol^{-1}	External CO_2 concentration at the upper surface of the leaf boundary layer
g_{bCO_2}	mol m^{-2} s^{-1}	Quasi-laminar boundary layer conductance to CO_2
C_z	nmol O_3 m^{-3}	O_3 concentration at reference height (z)
C_l	nmol O_3 m^{-3}	O_3 concentration at the upper surface of the laminar layer of a leaf
g_{O_3}	mmol O_3 m^{-2} PLA s^{-1}	Stomatal conductance to O_3
$g_{O_{3m/s}}$	m s^{-1}	Stomatal conductance to O_3
g_{ext}	m s^{-1}	External conductance
r_c	s m^{-1}	Leaf surface resistance to O_3
r_{b,O_3}	s m^{-1}	Quasi-laminar leaf boundary layer resistance to O_3
r_a	s m^{-1}	Atmospheric resistance to O_3
r_{inc}	s m^{-1}	In-canopy resistance to O_3
r_{ext}	s m^{-1}	External plant cuticle resistance to O_3
r_{sto}	s m^{-1}	Stomatal resistance to O_3
u_z	m s^{-1}	Wind speed at a reference height z
u_l	m s^{-1}	Wind speed at the upper surface of the laminar layer of a leaf
L	m	Cross-wind leaf dimension
LAI	m^2 m^{-2}	Leaf area index
$PAR_{dir,i}$	W m^{-2}	Direct PAR in canopy layer i
$PAR_{diff,i}$	W m^{-2}	Diffuse PAR in canopy layer i
PAR_{total}	W m^{-2}	Direct and diffuse PAR at the top of the canopy
NPP	kg C m^{-2}	Net primary productivity
GPP	kg C m^{-2}	Gross primary productivity
R_p	kg C m^{-2}	Plant respiration
R_{pm}	kg C m^{-2}	Plant maintenance respiration
R_{pg}	kg C m^{-2}	Plant growth respiration
A_{netc}	kg C m^{-2}	Canopy net photosynthesis
R_{dc}	kg C m^{-2}	Non-water-stressed canopy dark respiration
$f_{sw} R_{dc}$	kg C m^{-2}	Water-stressed modified canopy dark respiration
C_{root}	kg C m^{-2}	Root C pool
C_{leaf}	kg C m^{-2}	Leaf C pool
C_{stem}	kg C m^{-2}	Stem C pool
C_{resv}	kg C m^{-2}	Reserve C pool
C_{harv}	kg C m^{-2}	Harvest pool
P_{root}	–	Root C pool partition coefficient
P_{leaf}	–	Leaf C pool partition coefficient
P_{stem}	–	Stem C pool partition coefficient
P_{resv}	–	Reserve C pool partition coefficient
P_{harv}	–	Harvest C pool partition coefficient
$C_{leaf,green}$	kg C m^{-2}	Green leaf C
$C_{leaf,brown}$	kg C m^{-2}	Brown leaf C
SLA	m^2 kg^{-1}	Specific leaf area
h	m	Crop height
$Yield_{grain}$	g C m^{-2}	Grain yield
k'_b	–	Beam and scattered beam PAR extinction coefficient
k_d'	–	Diffuse and scattered diffuse PAR extinction coefficient

Table A1. Continued.

Variable	Unit	Description
ρ_{cb}	–	Canopy refection coefficient for beam PAR
ρ_{cd}	–	Canopy reflection coefficient for diffuse PAR
β	radians	Solar elevation angle
δ	radians	Solar declination angle
PAR_{dir} (LAI)	$\mu mol\ m^{-2}\ s^{-1}$	Absorbed beam plus scattered beam PAR per unit leaf area
PAR_{diff} (LAI)	$\mu mol\ m^{-2}\ s^{-1}$	Absorbed diffuse plus scattered diffuse PAR per unit leaf area
PAR (LAI)	$\mu mol\ m^{-2}\ s^{-1}$	Total absorbed PAR per unit leaf area
I_b (LAI)	$\mu mol\ m^{-2}\ s^{-1}$	Direct PAR per unit ground area
I_d (LAI)	$\mu mol\ m^{-2}\ s^{-1}$	Diffuse PAR per unit ground area
I_d (0)	$\mu mol\ m^{-2}\ s^{-1}$	Diffuse PAR per unit ground area at the top of the canopy
I_b (0)	$\mu mol\ m^{-2}\ s^{-1}$	Beam PAR per unit ground area at the top of the canopy
PAR_{bs} (LAI)	$\mu mol\ m^{-2}\ s^{-1}$	Absorbed scattered beam PAR per unit leaf area
PAR_{bsun} (LAI)	$\mu mol\ m^{-2}\ s^{-1}$	Beam PAR absorbed by sunlit leaves per unit leaf area
PAR_{sh} (LAI)	$\mu mol\ m^{-2}\ s^{-1}$	Beam PAR absorbed by shaded leaves per unit leaf area
PAR_{sun} (LAI)	$\mu mol\ m^{-2}\ s^{-1}$	Total PAR absorbed by sunlit leaves per unit leaf area
PAR_{total}	$\mu mol\ m^{-2}\ s^{-1}$	Total absorbed irradiance per unit leaf area
LAI	$m^2\ m^{-2}$	Cumulative leaf area index from top of canopy ($L = 0$ at top)
$f1, 2$ (LAI)	–	Fraction of leaf area in a leaf-angle class
LAIsh	–	Fraction of leaves that are shaded
LAIsun	–	Fraction of leaves that are sunlit
σ	–	Leaf scattering coefficient for PAR
α_1	radians	Angle of beam irradiance to the leaf normal
$\sin\beta$	–	Solar elevation angle
k'_b	–	Beam and scattered beam PAR extinction coefficient
k_d'	–	Diffuse and scattered diffuse PAR extinction coefficient
σ	–	Leaf scattering coefficient for PAR
α_1	radians	Angle of beam irradiance to the leaf normal

Table A2. DO_3SE-Crop parameters for wheat. DO_3SE-Crop parameters for wheat, including default values. The table includes associated ranges only for parameters that require calibration under varying environmental conditions.

Parameter	Unit	Default value	Description	Reference	Range	Calibrated parameter value
T_b	°C	0	Base temperature	Tao et al. (2012); Osborne et al. (2015)	−0.5–1	−0.25
T_o	°C	20	Optimum temperature	Tao et al. (2012); Osborne et al. (2015)	15–25	17.79
T_m	°C	30	Maximum temperature	Tao et al. (2012); Osborne et al. (2015)	25–40	23.87
TT_{emr}	°C d	100	Thermal time between sowing and emergence	Lu and Fan (2013)	50–100	220.6
TT_{veg}	°C d	940	Thermal time between emergence and anthesis	Xiaoji experimental dataset	400–940	940
TT_{rep}	°C d	304	Thermal time between anthesis and maturity	Wang et al. (2013); Xiaoji experimental dataset	300–650	304
TT_{leaf}	°C d	1000	Total canopy leaf life span of the crop, covers period from emergence to maturity, distributed over the DVI between 0 and 2	Lu et al. (2018); Luo et al. (2020)	700–1200	795
T_l	°C d	1400	Total lifespan of the crop, covers the full period from sowing to maturity, corresponding to DVI between −1 and 2	Ewert and Porter (2000); Lu et al. (2018, 2020)	1300–1500	Year 2007–1325, year 2008–1400, year 2009–1478
PIV		1.5	Vernalisation coefficient	Tao et al. (2012); Wang et al. (2013)	2.9–4	2.9
PID		40	Photoperiod coefficient	Wang et al. (2013); Liu et al. (2016); Zhao et al. (2020)	40–57	40
VT_{max}	°C	30	Maximum daily temperature for vernalisation	Zheng et al. (2015)		
VT_{min}	°C	15	Minimum daily temperature for vernalisation	Zheng et al. (2015)		

Table A2. Continued.

Parameter	Unit	Default value	Description	Reference	Range	Calibrated parameter value
PAW_t	$m^3\ m^{-3}$	50	Plant available soil water below which stomatal conductance will start to reduce	LRTAP (2017)		
V_{cmax}	$\mu mol\ CO_2\ m^{-2}\ s^{-1}$	90	Maximum carboxylation capacity at 25 °C	Büker et al. (2012)	90–140	137
J_{max}	$\mu mol\ CO_2\ m^{-2}\ s^{-1}$	180	Maximum rate of electron transport at 25 °C	Büker et al. (2012)	180–250	228
K_c	$\mu mol\ mol^{-1}$	404.9	Rubisco Michaelis–Menten constants for CO_2	Medlyn et al. (2002)		
K_0	$mmol\ mol^{-1}$	278.4	Rubisco Michaelis–Menten constants for O_2	Medlyn et al. (2002)		
Γ^*	$\mu mol\ mol^{-1}$	42.75	CO_2 compensation point in the absence of respiration	Medlyn et al. (2002)		
a	–	4	Electron requirement for the formation of NADPH	Sharkey et al. (2007)		
b	–	8	Electron requirement for the formation of ATP	Sharkey et al. (2007)		
R_{dcoeff}	–	0.015	Leaf dark respiration coefficient	Clark et al. (2011)	0.010–0.03	0.01
f_{min}	$\mu mol\ CO_2\ m^2\ s^{-1}$	1000	Minimum daytime stomatal conductance to CO_2	Ewert and Porter (2000)		
m	–	7	Composite sensitivity slope constant	Büker et al. (2012)	4–15	5
VPD_0	kPa	2.2	Stomatal conductance sensitivity to VPD	LRTAP (2017); Pande et al. (2024)		
$\gamma 1$	–	0.027	O_3 short-term damage coefficient	Ewert and Porter (2000)		
$\gamma 2$	$(nmol\ O_3\ m^{-2}\ s^{-1})^{-1}$	0.0045	O_3 short-term damage coefficient	Ewert and Porter (2000)		
$\gamma 3$	$(\mu mol\ O_3\ m^{-2})^{-1}$	0.00005	O_3 long-term damage coefficient	Ewert and Porter (2000)	0.00001–0.00009	Tolerant = 0.00001; sensitive = 0.00002
$\gamma 4$	–	5	O_3 long-term damage coefficient determining onset of senescence		5–15	Tolerant = 5; sensitive = 15
$\gamma 5$	–	0.8	O_3 long-term damage coefficient determining maturity		0.5–5	Tolerant = 0.8; sensitive = 5
CLsO3	$mmol\ O_3\ m^{-2}$	6.5–20.6, 20.5	Critical accumulated stomatal O_3 flux that determines the onset of leaf senescence	Osborne et al. (2019); Y. Feng et al. (2022)	3–21	4.2

Table A2. Continued.

Parameter	Unit	Default value	Description	Reference	Range	Calibrated parameter value
r_{ext}	$m\,s^{-1}$	2500	External leaf cuticular resistance to O_3 uptake	LRTAP (2017)		
L	m	0.02	Cross-wind leaf dimension for wheat	LRTAP (2017)		
P_{st}	Pa	1.013×10^5	Standard air pressure at 20 °C	LRTAP (2017)		
T_{st}	°C	20	Standard temperature	LRTAP (2017)		
R	$J\,mol^{-1}\,K^{-1}$	8.31447	Universal gas constant	LRTAP (2017)		
n_e	$mol\,CO_2\,m^{-2}\,s^{-1}\,kg\,C\,(kg\,N)^{-1}$	0.0008	Constant relating leaf nitrogen to rubisco carboxylation capacity	Clark et al. (2011)		
n_0	$kg\,N\,[kg\,C]^{-1}$	0.073	Top of canopy leaf N concentration	Clark et al. (2011)		
kN		0.78	Nitrogen profile coefficient	Clark et al. (2011)		
R_{gcoeff}	–	0.25	Plant growth respiration coefficient	Osborne et al. (2015)	0.15–0.25	0.16
α_{root}	–	18.5	Coefficient for determining partitioning	Osborne et al. (2015)	16–19	18.4
α_{stem}	–	16.0	Coefficient for determining partitioning	Osborne et al. (2015)	16–17	16.8
α_{leaf}	–	18.0	Coefficient for determining partitioning	Osborne et al. (2015)	18–19	18.5
β_{root}	–	−20.0	Coefficient for determining partitioning	Osborne et al. (2015)	20–21	−20.9
β_{stem}	–	−15.0	Coefficient for determining partitioning	Osborne et al. (2015)	14–16	−14.5
β_{leaf}	–	−18.5	Coefficient for determining partitioning	Osborne et al. (2015)	18–19	−18.11
f_c	–	0.5	Carbon fraction of dry matter	Osborne et al. (2015)		
Υ	$m^{-2}\,kg^{-1}$	27.3	Coefficient for determining specific leaf area	Osborne et al. (2015)	13–28	13.5
δ	–	−0.0507	Coefficient for determining specific leaf area	Osborne et al. (2015)		
k	–	1.4	Allometric coefficient which relates C_{stem} to h	Osborne et al. (2015)		

Table A2. Continued.

Parameter	Unit	Default value	Description	Reference	Range	Calibrated parameter value
τ	–	0.4	Allometric coefficient which relates C_{stem} to h	Osborne et al. (2015)	0.3–0.6	0.4
D_w	–	1/0.84	Conversion factor to allow for grain moisture content	Mulvaney and Devkota (2020)		
E_g	–	0.85	Conversion factor for grain-to-ear ratio	Nagarajan et al. (1999); Kutman et al. (2011)		
R_{SL}	–	2 : 1	Stem dry matter to leaf dry matter ratio	Huang et al. (2022)		
k'_b	–	$0.46/\sin\beta$	Beam and scattered beam PAR extinction coefficient	de Pury and Farquhar (1997)		
k_d'	–	0.8	Diffuse and scattered diffuse PAR extinction coefficient	de Pury and Farquhar (1997)		
σ	–	0.15	Leaf scattering coefficient for PAR	de Pury and Farquhar (1997)		
α_1	radians	0.5	Angle of beam irradiance to the leaf normal	de Pury and Farquhar (1997)		

Code availability. An open version (version 4.39.16) of the DO_3SE-Crop model, as used in the present study, can be found on both https://doi.org/10.5281/zenodo.11620482 and https://github.com/DO3SE/pyDO3SE-open/tree/v4.39.16, last access: 11 June 2024 (Bland, 2024).

Data availability. The datasets referred to in this study are not publicly accessible. These data were obtained from third-party sources under specific usage agreements. Researchers interested in accessing these datasets should contact the respective data providers directly.

Supplement. The supplement related to this article is available online at: https://doi.org/10.5194/bg-22-181-2025-supplement.

Author contributions. PP, LE, and ZF: conceptualisation. PP and ZF: data curation. PP: formal analysis. PP, LE, and ZF: methodology. PP, SB, NB, JC, and LE: software – DO_3SE-Crop. LE and ZF: supervision. PP: visualisation and writing – original draft preparation. PP, SB, NB, JC, ZF, and LE: writing – review and editing.

Competing interests. The contact author has declared that none of the authors has any competing interests.

Disclaimer. Publisher's note: Copernicus Publications remains neutral with regard to jurisdictional claims made in the text, published maps, institutional affiliations, or any other geographical representation in this paper. While Copernicus Publications makes every effort to include appropriate place names, the final responsibility lies with the authors.

Special issue statement. This article is part of the special issue "Tropospheric Ozone Assessment Report Phase II (TOAR-II) Com-

munity Special Issue (ACP/AMT/BG/GMD inter-journal SI)". It is a result of the Tropospheric Ozone Assessment Report, Phase II (TOAR-II, 2020–2024).

Acknowledgements. We would like to thank the anonymous reviewers for their insightful comments and suggestions, which helped clarify and improve the quality of this paper.

Financial support. This research has been financially supported by the Science and Technology Facilities Council (STFC) research grant (ST/V002481/1) for the "Pollution and Climate Smart Agriculture in China" (PaCSAC) project which supported initial development of the DO_3SE-Crop model. Support from the Royal Society through the International Exchanges 2021 Cost Share (NSFC) grant (IEC\NSFC\211154) facilitated the UK–China collaboration to parameterise the DO_3SE-Crop model within the project "Understanding the role of air pollution and climate on staple crop yields and nutrition in China". We also received support from the STFC research grant (ST/Y005317/1) under the EO4AgroClimate programme for the project "Towards a digital twin of cropping systems based on ingestion of EO into process-based crop models" which helped refine the DO_3SE-Crop model for a broader set of country applications.

Review statement. This paper was edited by Paul Stoy and reviewed by three anonymous referees.

References

Amthor, J. S., Bar-Even, A., Hanson, A. D., Millar, A. H., Stitt, M., Sweetlove, L. J., and Tyerman, S. D.: Engineering strategies to boost crop productivity by cutting respiratory carbon loss, Plant Cell, 31, 297–314, https://doi.org/10.1105/tpc.18.00743, 2019.

Betzelberger, A. M., Gillespie, K. M., McGrath, J. M., Koester, R. P., Nelson, R. L., and Ainsworth, E. A.: Ozone exposure response for U.S. soybean cultivars: Linear reductions in photosynthetic potential, biomass, and yield, Plant Physiology, American Society of Plant Biologists, 160, 1827–1839, https://doi.org/10.1104/pp.112.205591, 2012.

Beven, K.: A manifesto for the equifinality thesis, J. Hydrol., 320, 18–36, https://doi.org/10.1016/j.jhydrol.2005.07.007, 2006.

Biswas, D. K., Xu, H., Li, Y. G., Sun, J. Z., Wang, X. Z., Han, X. G., and Jiang, G. M.: Assessing the genetic relatedness of higher ozone sensitivity of modern wheat to its wild and cultivated progenitors/relatives, J. Exp. Bot., 59, 951–963, https://doi.org/10.1093/jxb/ern022, 2008.

Bland, S.: SEI-DO3SE/pyDO3SE-open: V4.39.11 (v4.39.11), Zenodo [code], https://doi.org/10.5281/zenodo.11620482, 2024.

Brewster, C., Fenner, N., and Hayes, F.: Chronic ozone exposure affects nitrogen remobilization in wheat at key growth stages, Sci. Total Environ., 908, 168288, https://doi.org/10.1016/j.scitotenv.2023.168288, 2024.

Büker, P., Morrissey, T., Briolat, A., Falk, R., Simpson, D., Tuovinen, J.-P., Alonso, R., Barth, S., Baumgarten, M., Grulke, N., Karlsson, P. E., King, J., Lagergren, F., Matyssek, R., Nunn, A., Ogaya, R., Peñuelas, J., Rhea, L., Schaub, M., Uddling, J., Werner, W., and Emberson, L. D.: DO_3SE modelling of soil moisture to determine ozone flux to forest trees, Atmos. Chem. Phys., 12, 5537–5562, https://doi.org/10.5194/acp-12-5537-2012, 2012.

Campbell, G. S. and Norman, J. M.: An introduction to Environmental Biophysics, Second Edition, Springer, New York, 286 pp., https://doi.org/10.1007/978-1-4612-1626-1, 1998.

Clark, D. B., Mercado, L. M., Sitch, S., Jones, C. D., Gedney, N., Best, M. J., Pryor, M., Rooney, G. G., Essery, R. L. H., Blyth, E., Boucher, O., Harding, R. J., Huntingford, C., and Cox, P. M.: The Joint UK Land Environment Simulator (JULES), model description – Part 2: Carbon fluxes and vegetation dynamics, Geosci. Model Dev., 4, 701–722, https://doi.org/10.5194/gmd-4-701-2011, 2011.

Conibear, L., Butt, E. W., Knote, C., Spracklen, D. V., and Arnold, S. R.: Current and Future Disease Burden From Ambient Ozone Exposure in India, GeoHealth, 2, 334–355, https://doi.org/10.1029/2018GH000168, 2018.

Danielsson, H., Karlsson, G. P., Karlsson, P. E., and Pleijel, H. H.: Ozone uptake modelling and flux-response relationships–an assessment of ozone-induced yield loss in spring wheat, Atmos. Environ., 37, 475–485, https://doi.org/10.1016/S1352-2310(02)00924-X, 2003.

de Pury, D. G. G. and Farquhar, G. D.: Simple Scaling of Photosynthesis from Leaves to Canopies Without the Errors of Big-Leaf Models, Funct. Plant Biol., 24, 537–557, https://doi.org/10.1111/j.1365-3040.1997.00094.x, 1997.

Droutsas, I., Challinor, A. J., Arnold, S. R., Mikkelsen, T. N., and Hansen, E. M. Ø.: A new model of ozone stress in wheat including grain yield loss and plant acclimation to the pollutant, Eur. J. Agron., 120, 126125, https://doi.org/10.1016/j.eja.2020.126125, 2020.

Emberson, L. D., Ashmore, M. R., Cambridge, H. M., Simpson, D., and Tuovinen, J.-P.: Modelling stomatal ozone flux across Europe, Environ. Pollut., 109, 403–413, https://doi.org/10.1016/S0269-7491(00)00043-9, 2000.

Emberson, L. D., Ashmore, M. R., Simpson, D., Tuovinen, J.-P., and Cambridge, H. M.: Modelling and mapping ozone deposition in Europe, Water Air Soil Poll., 577–582, 2001.

Emberson, L. D., Pleijel, H., Ainsworth, E. A., van den Berg, M., Ren, W., Osborne, S., Mills, G., Pandey, D., Dentener, F., Büker, P., Ewert, F., Koeble, R., and Van Dingenen, R: Ozone effects on crops and consideration in crop models, Eur. J. Agron., 100, 19–34, https://doi.org/10.1016/j.eja.2018.06.002, 2018.

Ewert, F. and Porter, J. R.: Ozone effects on wheat in relation to CO_2: Modelling short-term and long-term responses of leaf photosynthesis and leaf duration, Glob. Change Biol., 6, 735–750, https://doi.org/10.1046/j.1365-2486.2000.00351.x, 2000.

Farage, P. K., Long, S. P., Lechner, E. G., and Baker, N. R.: The sequence of change within the photosynthetic apparatus of wheat following short-term exposure to ozone, Plant Physiol., 95, 529–535, https://doi.org/10.1104/pp.95.2.529, 1991.

Farquhar, G. D., von Caemmerer, S., and Berry, J. A.: A biochemical model of photosynthetic CO_2 assimilation in leaves of C3 species, Planta, 149, 78–90, https://doi.org/10.1007/BF00386231, 1980.

Feng, Y., Nguyen, T. H., Alam, M. S., Emberson, L., Gaiser, T., Ewert, F., and Frei, M: Identifying and modelling key physiological traits that confer tolerance or sensitivity to ozone in win-

ter wheat, Environmental Pollution, Elsevier Ltd, 304, 119251, https://doi.org/10.1016/j.envpol.2022.119251, 2022.

Feng, Y., Alam, M. S., Yan, F., and Frei, M.: Alteration of carbon and nitrogen allocation in winter wheat under elevated ozone, Plant Sci., 338, 111924, https://doi.org/10.1016/j.plantsci.2023.111924, 2024.

Feng, Z., Kobayashi, K., and Ainsworth, E. A.: Impact of elevated ozone concentration on growth, physiology, and yield of wheat (Triticum aestivum L.): a meta-analysis, Glob. Change Biol., 14, 2696–2708, https://doi.org/10.1111/j.1365-2486.2008.01673.x, 2008.

Feng, Z., Pang, J., Kobayashi, K., Zhu, J., and Otr, R. D.: Differential responses in two varieties of winter wheat to elevated ozone concentration under fully open-air field conditions, Glob. Change Biol., 17, 580–591, https://doi.org/10.1111/j.1365-2486.2010.02184.x, 2011.

Feng, Z., Tang, H., Uddling, J., Pleijel, H., Kobayashi, K., Zhu, J., Oue, H., and Guo, W.: A stomatal ozone flux-response relationship to assess ozone-induced yield loss of winter wheat in subtropical China, Environ. Pollut., 164, 16–23, https://doi.org/10.1016/j.envpol.2012.01.014, 2012.

Feng, Z., Wang, L., Pleijel, H., Zhu, J., and Kobayashi, K.: Differential effects of ozone on photosynthesis of winter wheat among cultivars depend on antioxidative enzymes rather than stomatal conductance, Sci. Total Environ., 572, 404–411, https://doi.org/10.1016/j.scitotenv.2016.08.083, 2016.

Feng, Z., Uddling, J., Tang, H., Zhu, J., and Kobayashi, K.: Comparison of crop yield sensitivity to ozone between open-top chamber and free-air experiments, Glob. Change Biol., 24, 2231–2238, https://doi.org/10.1111/gcb.14077, 2018.

Feng, Z., Agathokleous, E., Yue, X., Oksanen, E., Paoletti, E., Sase, H., Gandin, A., Koike, T., Calatayud, V., Yuan, X., Liu, X., De Marco, A., Jolivet, Y., Kontunen-Soppela, S., Hoshika, Y., Saji, H., Li, P., Li, Z., Watanabe, M., and Kobayashi, K.: Emerging challenges of ozone impacts on Asian plants: Actions are needed to protect ecosystem health, Ecosystem Health and Sustainability, 7, 1911602. https://doi.org/10.1080/20964129.2021.1911602, 2021.

Feng, Z., Xu, Y., Kobayashi, K., Dai, L., Zhang, T., Agathokleous, E., Calatayud, V., Paoletti, E., Mukherjee, A., Agrawal, M., Park, R. J., Oak, Y. J., and Yue, X.: Ozone pollution threatens the production of major staple crops in East Asia, Nature Food, 3, 47–56, https://doi.org/10.1038/s43016-021-00422-6, 2022.

Gelang, J., Pleijel, H., Sild, E., Danielsson, H., Younis, S., Selldén, G., and Wallin, G.: Rate and duration of grain filling in relation to flag leaf senescence and grain yield in spring wheat (Triticum aestivum) exposed to different concentrations of ozone, Physiol. Plantarum, 110, 366–375, https://doi.org/10.1111/j.1399-3054.2000.1100311.x, 2000.

Grandjean, A. and Fuhrer, J.: Growth and leaf senescence in spring wheat (Triticum aestivum) grown at different ozone concentrations in open-top field chambers, Environ. Pollut., 59, 299–314, 1989.

Guan, X., Song, L., Wang, T. C., Turner, N., and Li, F.: Effect of Drought on the Gas Exchange, Chlorophyll Fluorescence and Yield of Six Different-Era Spring Wheat Cultivars, J. Agron. Crop Sci., 201, 253–266, https://doi.org/10.1111/jac.12103, 2015.

Guarin, J. R., Kassie, B., Mashaheet, A. M., Burkey, K., and Asseng, S.: Modeling the effects of tropospheric ozone on wheat growth and yield, Eur. J. Agron., 105, 13–23, https://doi.org/10.1016/j.eja.2019.03.001, 2019.

Guarin, J. R., Jägermeyr, J., Ainsworth, E. A., Oliveira, F. A. A., Asseng, S., Boote, K., Elliott, J., Emberson, L., Foster, I., Hoogenboom, G., Kelly, D., Ruane, A. C., and Sharps, K.: Modeling the effects of tropospheric ozone on the growth and yield of global staple crops with DSSAT v4.8.0, Geosci. Model Dev., 17, 2547–2567, https://doi.org/10.5194/gmd-17-2547-2024, 2024.

Herman, J. and Usher, W.: SALib: An open-source Python library for sensitivity analysis, J. Open Source Softw., 2, 97, https://doi.org/10.21105/joss.00097, 2017.

Huang, H., Huang, J., Li, X., Feng, J., Zhuo, W., Wu, Y., Niu, Q., Su, W., and Yin, Y.: A dataset of winter wheat aboveground biomass in China during 2007–2015 based on data assimilation, Scientific Data, Springer US, 9, 1–11, https://doi.org/10.1038/s41597-022-01305-6, 2022.

Hussain, A. and Bangash, R.: Impact of Climate Change on Crops' Productivity across Selected Agro-ecological Zones in Pakistan, The Pakistan Development Review, 56, 163–187, https://www.jstor.org/stable/26875191, 2017.

IPCC: Climate Change 2021: The Physical Science Basis. Contribution of Working Group I to the Sixth Assessment Report of the Intergovernmental Panel on Climate Change, Cambridge University Press, https://doi.org/10.1017/9781009157896, 2021.

Iwanaga, T., Usher, W., and Herman, J.: Toward SALib 2.0: Advancing the accessibility and interpretability of global sensitivity analyses, Socio-Environ. Syst. Model., 4, 18155, https://doi.org/10.18174/sesmo.18155, 2022.

Jaggi, M., Ammann, C., Neftel, J., and Fuhrer, J.: Environmental control of profiles of ozone concentration in a grassland canopy, Atmos. Environ., 40, 5496–5507, https://doi.org/10.1016/j.atmosenv.2006.01.025, 2006.

Jones, H. G.: Plants and microclimate: A quantitative approach to environmental plant physiology, Cambridge University Press, ISBN 0521425247, 1992.

Kohut, R. J., Amundson, R. G., Laurence, J. A., Colavito, L., van Leuken, P., and King, P.: Effects of Ozone and Sulfur Dioxide on Yield of Winter Wheat, Phytopathology, 77, 71–74, https://doi.org/10.1094/Phyto-77-71, 1987.

Kutman, U. B., Yildiz, B., and Cakmak, I.: Effect of nitrogen on uptake, remobilization and partitioning of zinc and iron throughout the development of durum wheat, Plant Soil, 342, 149–164, https://doi.org/10.1007/s11104-010-0679-5, 2011.

Lee, J. D., Drysdale, W. S., Finch, D. P., Wilde, S. E., and Palmer, P. I.: UK surface NO_2 levels dropped by 42

Leung, F., Williams, K., Sitch, S., Tai, A. P. K., Wiltshire, A., Gornall, J., Ainsworth, E. A., Arkebauer, T., and Scoby, D.: Calibrating soybean parameters in JULES 5.0 from the US-Ne2/3 FLUXNET sites and the SoyFACE-O3 experiment, Geosci. Model Dev., 13, 6201–6213, https://doi.org/10.5194/gmd-13-6201-2020, 2020.

Leuning, R.: Modeling stomatal behavior and photosynthesis of Eucalyptus grandis, Aust. J. Plant Physiol., 17, 159–175, 1990.

Leuning, R.: A critical appraisal of combined stomatal models for C3 plants, Plant, Cell Environ., 18, 339–355, 1995.

Li, A., Zhou, Q., and Xu, Q.: Prospects for ozone pollution control in China: An epidemiological perspective, Environ. Pollut., 285, 117670, https://doi.org/10.1016/j.envpol.2021.117670, 2021.

Li, D., Shindell, D., Ding, D., Lu, X., Zhang, L., and Zhang, Y.: Surface ozone impacts on major crop production in China from 2010 to 2017, Atmos. Chem. Phys., 22, 2625–2638, https://doi.org/10.5194/acp-22-2625-2022, 2022.

Li, K., Jacob, D. J., Shen, L., Lu, X., De Smedt, I., and Liao, H.: Increases in surface ozone pollution in China from 2013 to 2019: anthropogenic and meteorological influences, Atmos. Chem. Phys., 20, 11423–11433, https://doi.org/10.5194/acp-20-11423-2020, 2020.

Lim, P. O., Kim, H. J., and Nam, H. G.: Leaf senescence, Annu. Rev. Plant Biol., 58, 115–136, https://doi.org/10.1146/annurev.arplant.57.032905.105316, 2007.

Lin, M., Horowitz, L. W., Payton, R., Fiore, A. M., and Tonnesen, G.: US surface ozone trends and extremes from 1980 to 2014: quantifying the roles of rising Asian emissions, domestic controls, wildfires, and climate, Atmos. Chem. Phys., 17, 2943–2970, https://doi.org/10.5194/acp-17-2943-2017, 2017.

Liu, B., Asseng, S., Liu, L., Tang, L., Cao, W., and Zhu, Y.: Testing the responses of four wheat crop models to heat stress at anthesis and grain filling, Glob. Change Biol., 22, 1890–1903, https://doi.org/10.1111/gcb.13212, 2016.

Liu, S., Mo, X., Lin, Z., Xu, Y., Ji, J., Wen, G., and Richey, J.: Crop yield responses to climate change in the Huang-Huai-Hai Plain of China, Agr. Water Manage., 97, 1195–1209, https://doi.org/10.1016/j.agwat.2010.03.012, 2010.

Liu, Z., Doherty, R. M., Wild, O., O'Connor, F. M., and Turnock, S. T.: Tropospheric ozone changes and ozone sensitivity from the present day to the future under shared socioeconomic pathways, Atmos. Chem. Phys., 22, 1209–1227, https://doi.org/10.5194/acp-22-1209-2022, 2022.

LRTAP: Mapping critical levels for vegetation, chapter III of manual on methodologies and criteria for modelling and mapping critical loads and levels and air pollution effects, risks and trends, UNECE Convention on Long-range Transboundary Air Pollution, 2017.

Lu, C. and Fan, L.: Winter wheat yield potentials and yield gaps in the North China Plain, Field Crops Res., 143, 98–105, https://doi.org/10.1016/j.fcr.2012.09.015, 2013.

Luo, Y., Zhang, Z., Li, Z., Chen, Y., Zhang, L., Cao, J., and Tao, F.: Identifying the spatiotemporal changes of annual harvesting areas for three staple crops in China by integrating multi-data sources, Environ. Res. Lett., 15, 074003, https://doi.org/10.1088/1748-9326/ab80f0, 2020.

Luo, Y., Zhang, Z., Zhang, L., and Cao, J.: Spatiotemporal patterns of winter wheat phenology and its climatic drivers based on an improved pDSSAT model, Sci. China Earth Sci., 64, 2144–2160, https://doi.org/10.1007/s11430-020-9821-0, 2021.

Malhi, G. S., Kaur, M., and Kaushik, P.: Impact of Climate Change on Agriculture and Its Mitigation Strategies: A Review, Sustainability, 13, 1318, https://doi.org/10.3390/su13031318, 2021.

Mariën, B., Balzarolo, M., Dox, I., Leys, S., Marchand J. L., Géron, C., Portillo-Estrada, M., AbdElgawad, H., Asard, H., and Campioli, M.: Detecting the onset of autumn leaf senescence in deciduous forest trees of the temperate zone, New Phytol., 224, 166–176, https://doi.org/10.1111/nph.15991, 2019.

Masutomi, Y.: The appropriate analytical solution for coupled leaf photosynthesis and stomatal conductance models for C3 plants, Ecol. Model., 481, 110306, https://doi.org/10.1016/j.ecolmodel.2023.110306, 2023.

Medlyn, B. E., Dreyer, E., Ellsworth, D., Forstreuter, M., Harley, P., Kirschbaum, M., Roux, X., Montpied, P., Strassemeyer, J., Walcroft, A., Wang, K., and Loustau, D.: Temperature response of parameters of a biochemically based model of photosynthesis. II. A review of experimental data, Plant Cell Environ., 25, 1167–1179, https://doi.org/10.1046/j.1365-3040.2002.00891.x, 2002.

Miller, J. D., Arteca, R. N., and Pell, E. J.: Senescence-Associated Gene Expression during Ozone-Induced Leaf Senescence in Arabidopsis, Plant Physiol., 120, 1015, https://doi.org/10.1104/pp.120.4.1015, 1999.

Mulvaney, M. J. and Devkota, P. J.: Adjusting Crop Yield to a Standard Moisture Content, EDIS, University of Florida George A Smathers Libraries, https://doi.org/10.32473/edis-ag442-2020, 2020.

Nagarajan, S., Rane, J., Maheswari, M., and Gambhir, P. N.: Effect of Post-Anthesis Water Stress on Accumulation of Dry Matter, Carbon and Nitrogen and Their Partitioning in Wheat Varieties Differing in Drought Tolerance, J. Agron. Crop Sci., 183, 129–136, https://doi.org/10.1046/j.1439-037x.1999.00326.x, 1999.

Nguyen, T. H., Cappelli, G. A., Emberson, L., Ignacio, G. F., Irimescu, A., Francesco, S., Fabrizio, G., Booth, N., Boldeanu, G., Bermejo, V., Bland, S., Frei, M., Ewert, F., and Gaiser, T.: Assessing the spatio-temporal tropospheric ozone and drought impacts on leaf growth and grain yield of wheat across Europe through crop modeling and remote sensing data, Eur. J. Agron., 153, 127052, https://doi.org/10.1016/j.eja.2023.127052, 2024.

Okrah, A., Li, S., Agathokleous, E., and Feng, Z.: Elevated ozone effects on potato leaf physiology, growth, and yield: a meta-analysis, Environ. Sci. Pollut. Res., 30, 120483–120495, https://doi.org/10.1007/s11356-023-30854-5, 2023.

Osborne, S., Pandey, D., Mills, G., Hayes, F., Harmens, H., Gillies, D., Bücker, P., and Emberson, L.: New Insights into Leaf Physiological Responses to Ozone for Use in Crop Modelling, Plants, 8, 84, https://doi.org/10.3390/plants8040084, 2019.

Osborne, T., Gornall, J., Hooker, J., Williams, K., Wiltshire, A., Betts, R., and Wheeler, T.: JULES-crop: a parametrisation of crops in the Joint UK Land Environment Simulator, Geosci. Model Dev., 8, 1139–1155, https://doi.org/10.5194/gmd-8-1139-2015, 2015.

Pande, P., Hayes, F., Bland, S., Booth, N., Pleijel, H., and Emberson, L. D.: Ozone Dose-Response Relationships for Wheat Can Be Derived Using Photosynthetic-Based Stomatal Conductance Models, Agr. Forest Meteorol., 356, 110150, https://doi.org/10.1016/j.agrformet.2024.110150, 2024.

Penning de Vries, F. W. T.: Simulation of Ecophysiological Processes of Growth in Several Annual Crops, Simulation Monographs, Vol. 29, Netherlands Centre for Agricultural Publishing and Documentation, Int. Rice Res. Inst., 271 pp., ISBN 9022010007, 9789022010006, 1989.

Pleijel, H., Danielsson, H., Emberson, L., Ashmore, M., and Mills, G.: Ozone Risk Assessment for Agricultural Crops in Europe: Further Development of Stomatal Flux and Flux–Response Relationships for European Wheat and Potato, Atmos. Environ., 41, 3022–3040, https://doi.org/10.1016/j.atmosenv.2006.12.002, 2007.

Pleijel, H., Danielsson, H., and Broberg, M. C.: Benefits of the Phytotoxic Ozone Dose (POD) index in dose-response functions for wheat yield loss, Atmos. Environ., 268, 118797, https://doi.org/10.1016/j.atmosenv.2021.118797, 2022.

Qin, X., Zhang, F., Liu, C., Yu, H., Cao, B., Tian, S., Liao, Y., and Siddique, K.: Wheat Yield Improvements in China: Past Trends and Future Directions, Field Crops Res., 177, 117–124, https://doi.org/10.1016/j.fcr.2015.03.013, 2015.

Ronan, A. C., Ducker, J. A., Schnell, J. L., and Holmes, C. D.: Have improvements in ozone air quality reduced ozone uptake into plants?, Elem. Sci. Anth., 8, 2, https://doi.org/10.1525/elementa.399, 2020.

Schauberger, B., Rolinski, S., Schaphoff, S., and Müller, C.: Global Historical Soybean and Wheat Yield Loss Estimates from Ozone Pollution Considering Water and Temperature as Modifying Effects, Agr. Forest Meteorol., 265, 1–15, https://doi.org/10.1016/j.agrformet.2018.11.004, 2019.

Sharkey, T. D., Bernacchi, C. J., Farquhar, G. D., and Singsaas, E. L.: Fitting Photosynthetic Carbon Dioxide Response Curves for C3 Leaves, Plant Cell Environ., 30, 1035–1040, https://doi.org/10.1111/j.1365-3040.2007.01710.x, 2007.

Shi, G., Yang, L., Wang, Y., Kobayashi, K., Zhu, J., Tang, H., Pan, S., Chen, T., Liu, G., and Wang, Y.: Impact of elevated ozone concentration on yield of four Chinese rice cultivars under fully open-air field conditions, Agr. Ecosyst. Environ., 131, 178–184, https://doi.org/10.1016/j.agee.2009.01.009, 2009.

Sillmann, J., Aunan, K., Emberson, L., Bücker, P., van Oort, B. V., O'Neill, C., Otero, N., Pandey, D., and Brisebois, A.: Combined Impacts of Climate and Air Pollution on Human Health and Agricultural Productivity, Environ. Res. Lett., 16, 074001, https://doi.org/10.1088/1748-9326/ac1df8, 2021.

Silvestro, P. C., Pignatti, S., Yang, H., Yang, G., Pascucci, S., Castaldi, F., and Casa, R.: Sensitivity analysis of the AquaCrop and SAFY crop models for the assessment of water-limited winter wheat yield in regional scale applications, PLoS ONE, 12, e0187485, https://doi.org/10.1371/journal.pone.0187485, 2017.

Simpson, D., Benedictow, A., Berge, H., Bergström, R., Emberson, L. D., Fagerli, H., Flechard, C. R., Hayman, G. D., Gauss, M., Jonson, J. E., Jenkin, M. E., Nyíri, A., Richter, C., Semeena, V. S., Tsyro, S., Tuovinen, J.-P., Valdebenito, Á., and Wind, P.: The EMEP MSC-W chemical transport model – technical description, Atmos. Chem. Phys., 12, 7825–7865, https://doi.org/10.5194/acp-12-7825-2012, 2012.

Sitch, S., Cox, P. M., Collins, W. J., and Huntingford, C.: Indirect Radiative Forcing of Climate Change Through Ozone Effects on the Land-Carbon Sink, Nature, 448, 791–795, https://doi.org/10.1038/nature06059, 2007.

Tao, F., Zhang, S., and Zhang, Z.: Spatiotemporal changes of wheat phenology in China under the effects of temperature, day length and cultivar thermal characteristics, Eur. J. Agron., 43, 201–212, https://doi.org/10.1016/j.eja.2012.06.004, 2012.

Tao, F., Feng, Z., Tang, H., Chen, Y., and Kobayashi, K.: Effects of Climate Change, CO_2 and O_3 on Wheat Productivity in Eastern China, Singly and in Combination, Atmos. Environ., 153, 182–193, https://doi.org/10.1016/j.atmosenv.2017.01.032, 2017.

Triboi, E. and Triboi-Blondel, A. M.: Productivity and Grain or Seed Composition: A New Approach to an Old Problem – Invited Paper, Eur. J. Agron., 16, 163–186, https://doi.org/10.1016/S1161-0301(01)00146-0, 2002.

Van Oijen, M. and Ewert, F.: The effects of climatic variation in Europe on the yield response of spring wheat cv. Minaret to elevated CO_2 and O_3: an analysis of open-top chamber experiments by means of two crop growth simulation models, Eur. J. Agron., 10, 249–264, https://doi.org/10.1016/s1161-0301(99)00014-3, 1999.

Vazquez-Cruz, M. A. and Guzman, R.: Global sensitivity analysis by means of EFAST and Sobol' methods and calibration of the reduced state-variable TOMGRO model using genetic algorithms, Comput. Electron. Agric., 100, 1–12, https://doi.org/10.1016/j.compag.2013.10.006, 2014.

Wallach, D.: Crop model calibration: A statistical perspective. Agron. J., 103, 1141–1153, https://doi.org/10.2134/agronj2010.0432, 2011.

Wang, Q. J.: Using Genetic Algorithms to Optimise Model Parameters, Environ. Model. Softw., 12, 27–34, https://doi.org/10.1016/S1364-8152(96)00030-8, 1997.

Yadav, D. S., Mishra, A. K., Rai, R., Chaudhary, N., Mukherjee, A., Agrawal, S. B., and Agrawal, M.: Responses of an Old and a Modern Indian Wheat Cultivar to Future O_3 Levels: Physiological, Yield and Grain Quality Parameters, Environ. Pollut., 263, 113939, https://doi.org/10.1016/j.envpol.2020.113939, 2020.

Yang, L., Liu, S., Tsoka, S., and Papageorgiou, L. G.: Mathematical Programming for Piecewise Linear Regression Analysis, Expert Syst. Appl., 44, 156–167, https://doi.org/10.1016/j.eswa.2015.08.034, 2016.

Zhang, X., Xu, W., Zhang, G., Lin, W., Zhao, H., Ren, S., Zhou, G., Chen, J., and Xu, X.: First long-term surface ozone variations at an agricultural site in the North China Plain: Evolution under changing meteorology and emissions, Sci. Total Environ., 860, 160520, https://doi.org/10.1016/j.scitotenv.2022.160520, 2023.

Zhao, P., Zhou, Y., Li, F., Ling, X., Deng, N., Peng, S., and Man, J.: The Adaptability of APSIM-Wheat Model in the Middle and Lower Reaches of the Yangtze River Plain of China: A Case Study of Winter Wheat in Hubei Province, Agronomy, 10, 981, https://doi.org/10.3390/agronomy10070981, 2020.

Zheng, B., Chenu, K., Doherty, A., and Chapman, S.: The APSIM-Wheat Module (7.5 R3008), APSIM Initiative, 44 pp., https://www.apsim.info/documentation/model-documentation/crop-module-documentation/wheat/ (last access: 28 December 2024), 2015.

Zhu, X., Feng, Z., Sun, T., Liu, X., Tang, H., Zhu, J., Guo, W., and Kobayashi, K.: Effects of Elevated Ozone Concentration on Yield of Four Chinese Cultivars of Winter Wheat Under Fully Open-Air Field Conditions, Glob. Change Biol., 17, 2697–2706, https://doi.org/10.1111/j.1365-2486.2011.02400.x, 2011.